EXPERIMENTAL AND THEORETICAL PRESSURE STUDIES OF PERISTALTIC PUMPING

by

Eugene C. Eckstein

Submitted in Partial Fulfillment

of the Requirements for the

Degrees of

Bachelor of Science

and

Master of Science

at the

MASSACHUSETTS INSTITUTE OF

TECHNOLOGY

January, 1970

Signature of Author. .....
Department of Mechanical Engineering

Certified by.....
Thesis Supervisor

Accepted by.....
Chairman, Departmental Committee
on Graduate Students

EXPERIMENTAL AND THEORETICAL PRESSURE STUDIES OF PERISTALTIC PUMPING

by

Eugene C. Eckstein

Submitted to the Department of Mechanical Engineering

in partial fulfillment of the requirements

for the degrees of

Bachelor of Science and Master of Science

ABSTRACT

Two types of experiments were performed on two-dimensional peristaltic pumps. In one apparatus, the pressure was measured as a function of time in order to check the validity of the low Reynolds number theory. These experiments were inconclusive. In a second apparatus measurements of pressure rise per wavelength and time-mean flow were made over a broad range of Reynolds numbers, between 0.02 and 30. The results of this series of experiments are compared to a power-series solution of Jaffrin. The experiments show the expansion solution to be correct in nature, and accurate up to a Reynolds number of 10. Of equal interest is the fact that no appreciable deviation from the low Reynolds number theory is seen until after a Reynolds number of unity is reached.

Thesis Supervisor: Professor Ascher H. Shapiro
Title: Ford Professor of Engineering

Acknowledgement

I wish to thank Professor Shapiro for his advice and guidance which helped me complete this project. Professor Jaffrin also provided much support. Steven Weinberg provided constructive commentary throughout the course of the experiments. Thanks are due to David Palmer and Richard Fenner for their aid in the construction of the experimental apparatus. I also wish to thank Sara Rothchild who did the typing.

Table of Contents

List of Symbols

a	mean half distance between peristaltic walls
b	mean amplitude of peristaltic wave
c	wave speed
d	developing length
f	general function
h	function describing wall shape
k	resistance of reservoir connector
L	length of peristaltic motion
P	pressure
ΔP_λ	differential pressure between two points one wavelength apart
Q	flow in the lab/frame; $= \int_0^h U dY$
$\overline{Q}$	time net flow in the wave frame
q	flow in the wave frame; $= \int_0^h u dY$
R	non-dimensional resistance
Rey	Reynolds number, $\frac{a^2 c}{\lambda \nu}$
t	time
U	lab frame velocity in X direction
u	wave frame velocity in X direction
w	width of two-dimensional channel
X	direction parallel to the flow
Y	direction perpendicular to the flow

Θ $\bar{Q}/bc$, non-dimensional time net flow

θ X-ct, wall shape variable

λ wavelength

μ Newtonian viscosity

ν kinematic viscosity

Introduction

The transport of fluids in the ureter and gut are two examples of peristaltic pumps occurring in nature. In both cases rythmic contraction and relaxation of the vessel are used to propel the contents forward. Using these analogies it is easy to define peristaltic motion as a progressive wave motion producing fluid flow where the motion of the containing walls is perpendicular to the direction of flow. A man-made machine using peristaltic motion is the roller pump.

The fluid mechanics of low-Reynolds-number, long wavelength peristaltic pumping has been recently analyzed by Shapiro, Jaffrin, and Weinberg[1]. In addition, Jaffrin has completed a power-series expansion of the Navier-Stokes equations to predict the effects of increasing Reynolds number[2]. The low-Reynolds-number theory has been verified by measurement of the time-average flow versus the pressure rise per wavelength[3].

Two types of experiments are reported. Verification of velocity profiles predicted by the low-Reynolds-number theory is possible through measurement of the pressure at a point as a function of time. This type of experiment can provide a more sensitive verification than the earlier measurements of time-average quantities. In the other type of experiment, the change in pumping characteristics was determined as the Reynolds number increased from the low to the intermediate range. The results of these experiments provide an experimental check on Jaffrin's expansion solution. Of equal importance, the experimental results will show the limit of validity of the solution. Jaffrin has obtained a limit by comparison of the expansion solution with an exact solution for small amplitude peristaltic waves by Hanin.

The knowledge of the effects of intermediate Reynolds number of peristaltic pumping is relevant to modelling of the ureter since the Reynolds number of the flow in the ureter is of order one[4]. A model using only the low Reynolds number theory would be adequate if the effects of increased Reynolds number are small. Design calculations for roller pumps might also use such knowledge either to determine the accuracy of low-Reynolds-number approximations or actually to evaluate pump performance for intermediate Reynolds number.

Theory

The theory of peristaltic pumping for low Reynolds number is now well established[5]. This section presents the basic equations and results with which the experimental equipment was designed and with which experimental results will be compared. Figure 1 illustrates the variables and coordinates of the progressive two-dimensional infinite wave train used in the theory. The X-direction is parallel to the direction of wave progression; the X-axis will be referred to as the center line of the wave. Two ratios of geometric length are of importance. The first, ϕ, is defined as the amplitude of the wave, b, divided by the average distance, a, of the wave from the center line. The range of ϕ is from zero to one where $\phi = 0$ corresponds to a channel with parallel, straight walls and $\phi = 1$ to a channel whose walls touch at the minima. The second ratio is the average distance, a, of the wave from the center line divided by the wavelength, λ, and is assumed to be much less than one. The only restriction on the waveshape, h, of the wall is that it be a function of the quantity X-ct, which establishes the wave train as infinite and progressing in the positive X-direction. This form of waveshape allows for easy, direct change of reference from the laboratory frame of reference to the "wave frame", in which the observer moves with the wave at the wavespeed, c. In this latter frame the flow is a steady one for an infinite wavetrain. In calculations for illustration of the theory, the waveshape was assumed to be sinusoidal:

$$h = a + b \sin \frac{2\pi}{\lambda} (X-ct) \qquad \text{Eq. 1}$$

Using the velocities derived from a balance of pressure and viscous forces the appropriate Reynolds number has been shown to be $a^2c/\lambda\nu$.[5]

If the total instantaneous flow through any cross-section in the lab frame is denoted as Q, the continuity equation is

$$\frac{\partial Q}{\partial X} + \frac{\partial h}{\partial t} = 0 \qquad \text{Eq. 2}$$

Since h is a function of the quantity X-ct, this equation can be integrated to give

$$Q - ch = f(t) \qquad \text{Eq. 3}$$

However, the flow in the wave frame, q, is a constant since the flow in the wave frame is steady. In changing from the lab frame to the wave frame, a term, ch, equal to the flow caused by the observer moving with the wave at the wave speed, is subtracted from Q to get q, the flow at a cross-section in the wave frame. Then, by examining Equation 3 in light of the reference-frame transformation, it is seen that, for an infinite wave train, f(t) is equal to the constant flow q.

The assumptions of $a/\lambda << 1$ and inertial force equal to zero reduce the Navier-Stokes equation in the Y-direction to $\partial P/\partial Y = 0$. The pressure is then a function only of time and of distance in the X-direction. The boundary conditions of symmetry about the center line and no X-component of velocity at the wall, combined with the Navier-Stokes equation in the X-direction, lead to the result

$$\frac{\partial P}{\partial X} = -\frac{3\mu Q}{h^3} \qquad \text{Eq. 4}$$

at any cross section. If Q is substituted for Equation 3, and Equation 4 is integrated, f(t) for a finite number of waves can be evaluated provided that the pressures are known as functions of time at the two ends of the finite wave train. For constant-pressure reservoirs at the ends, the result takes the form

$$f(t) = \frac{\frac{2\pi(P_0-P_L)}{3\mu\lambda}}{\int_{-ct}^{L-ct} \frac{d(X-ct)}{h^3}} - \frac{\int_{-ct}^{L-ct} \frac{c\,d(X-ct)}{h^2}}{\int_{-ct}^{L-ct} \frac{d(X-ct)}{h^3}} \qquad \text{Eq. 5}$$

If the total length, L, is an integer number of wavelengths the integrals of Equation 5, and consequently f(t), are invariant with time due to the periodic nature of the integrands[6]. Thus, there is a great advantage to an experiment with an integer number of wavelengths. Besides the simplification of pressure calculations, since f(t) is a constant, experimental verification of the infinite-wave-train theory is possible.

Two experimentally significant relations between pressure and other variables may be devloped from Equation 4. The first is a relationship between the pressure rise per wavelength, defined as

$$\Delta P_\lambda = \int_X^{\lambda + X} \frac{\partial P}{\partial X}\, dX \quad , \qquad \text{Eq. 6}$$

and the time-mean flow in the laboratory frame, which equals

$$\overline{Q} = \frac{1}{T}\int_0^T Q\,dt = ac + f(o) \qquad \text{Eq. 7}$$

The constant value of f(t) for an infinite wavetrain or an integer wavelength wavetrain is denoted by f(o). Execution of the integrals of Equation 6 with substitutions from Equations 1, 4, 5, and 7 leads to

$$\frac{a^2}{\mu c \lambda} \Delta P_\lambda = \frac{3}{2} \frac{\phi^2}{(1-\phi^2)^{5/2}} \left[3 - \frac{2+\phi^2}{\phi} \Theta\right] \qquad \text{Eq. 8}$$

The time-average flow has been non-dimensionalized to the form $\Theta = \overline{Q}/bc$.

Since the purpose of a pump is to impose a pressure rise or to create a flow, pump performance is usually characterized by the maximum achievable levels of these quantities. For a specific amplitude ratio, ϕ, the maximum values of ΔP_λ and Θ occur at the intercepts of a $\Delta P_\lambda - \Theta$ graph. The values of these maxima can be determined from Equation 8 and are

$$\Delta P_{\lambda\ max} = \frac{9}{2} \frac{\mu c \lambda}{a^2} \frac{\phi^2}{(1-\phi^2)^{5/2}} \qquad \text{Eq. 9}$$

$$\Theta_{max} = \frac{3\phi}{2+\phi^2} \qquad \text{Eq. 10}$$

Although, for an infinite wavetrain the pressure differences between two points one wavelength apart is a function only of the time-mean flow, the pressure difference between two points not an integral number of wavelengths apart depends also upon time. The pressure difference can easily be derived by integration of Equation 4 between the desired points: for two points X2 and X1, the pressure difference at any time is

$$P_{X2} - P_{X1} = \int_{\frac{2\pi}{\lambda}(X1-ct)}^{\frac{2\pi}{\lambda}(X2-ct)} \frac{-3\mu c\lambda}{2\pi a^2} \left[\frac{1}{(h/a)^2} + \frac{(\phi\Theta-1)}{(h/a)^3} \right] d\left(\frac{2\pi}{\lambda}[X-ct]\right) \quad \text{Eq. 11}$$

Variation of the pressure difference with time occurs because of the waveshape, h. The right hand side of Equation 11 is constant with time only for (X2-X1) equal to an integral number of wavelengths. Since the variation of h with time is smooth, the resulting pressure difference will also be smooth. If the pressure difference is evaluated for successive times and then plotted versus time, curves of the form illustrated in Figure 2 are obtained. These curves are for $\phi = 0.5$, $\Theta/\Theta_{max} = 0.5$, and with h as described in Equation 1.

The effect of the Reynolds number being small but not zero has been theoretically predicted through a power-series expansion of the Navier-Stokes equations[7]. Only the results of the solution in the form of time-average characteristics, Θ and ΔP_λ, will be examined here. The expansion terms were grouped in the following manner;

$$\Delta P_\lambda = \Delta P_{\lambda 0} + Rey\ \Delta P_{\lambda 1} + Rey^2\ \Delta P_{\lambda 2} + \ldots. \quad \text{Eq. 12}$$

The zero order terms are obtained by neglecting all inertial forces. The resulting relationship between ΔP_λ and Θ is Equation 8. The nature of the solution is not changed by the first order terms since the relationship between $(\Delta P_{\lambda 0} + Rey\ \Delta P_{\lambda 1})$ and $(\Theta_0 + Rey\ \Theta_1)$ is exactly the relationship between $\Delta P_{\lambda 0}$ and Θ_0. The terms proportional to Reynolds number squared show a deviation from the linear relationship. Figure 3 illustrates graphically the value of $\Delta P_{\lambda 2}$ as a function of the time-

average flow. The flow axis is normalized with respect to the maximum time-average flow when the Reynolds number is zero. The most interesting point of this graph is that, for $\phi > 0.4$, increasing the Reynolds number increases the pressure rise per wavelength if the time-average flow is small. A Reynolds number of approximately 20 is necessary for this effect to be appreciable. For $\phi < 0.4$ the pressure rise per wavelength always decreases for increasing Reynolds number. The solid-line curves of Figures 16 and 17 illustrate the theoretical effect of Reynolds number on the variables $\Delta P_{\lambda max}$ and $\mathcal{O}_{max}$ for $\phi = 0.7$.

Experimental Apparatus

This section contains descriptions of two apparatus which were used to perform separate sets of experiments. The apparatus used to measure pressure as a function of time will be called "apparatus number one". "Apparatus number two" will be used to denote the machine used to measure the effect of Reynolds number on ΔP_λ and $\bar{Q}$. The first part of this section contains information common to both apparatus and therefore has no heading. Subsequent parts deal only with one apparatus and are identified by a heading with the name of the apparatus.

The pumping section was part of an annulus with reservoirs at each end. In cylindrical coordinates the flow was parallel to the circumferential direction, the motion of the wall to the radial direction, and the width of the two-dimensional flow to the axial direction. Good accuracy of the approximation of a linear pump by an annular pump is dependent upon a small ratio of gap width to the radius of the annulus. The outer wall of the annulus was fixed while a peristaltic motion was imposed on the inner wall. For a linear, long wavelength, low Reynolds number peristaltic pump, a coordinate change in the Y-direction is the only difference between a pump with one wall undergoing motion and a pump with two moving walls each undergoing the same motion with half the amplitude. The centerline best illustrates the nature of the coordinate change. In the pump with two moving walls the centerline will be straight while in the pump with one moving wall the centerline will be a wave with half the amplitude of the wave in the moving wall and in phase with the moving wall. This pump geometry was chosen for its simplicity of construction while closely modelling the theory.

The method of imposing the peristaltic motion on the inner wall is illustrated schematically in Figure 4. In the center of the machine is a flexible-band cam with an even number of wave shapes on its perimeter. The cam imposes its shape on the moving wall; specific means of accomplishing this are discussed on pages 16 and 19. A rigid frame holds the stationary wall relative to the center of the cam. The moving wall is prevented from moving in the direction of the flow, i.e., rotating, by the frame. When the cam turns, the moving wall must move radially since it cannot rotate yet must conform to the wave shape on the periphery of the cam. The motion is of peristaltic type because the wave is progressive and the motion of the walls is perpendicular to the direction of the wave progression. The accuracy of this method of creating peristaltic motion is dependent on precise alignment of the cylindrical axis of the stationary wall and the axis of the cam and upon the accuracy of the waveshapes on the periphery of the cam.

Apparatus Number One. This section contains information pertinent to the machine on which the pressure-time measurements were taken. The mechanism used to impose the shape of the cam on the moving wall is shown in Figure 5. The moving wall was supported and guided by roller assemblies. The roller assemblies were mounted on rods extending radially into the cam so different wave shapes could be set on the cam periphery. The axis of revolution of the axle passed through the moving wall; this prevented the roller assemblies from exerting a moment on the wall. Each roller assembly could revolve on an axle through the rod (See Fig. 5). Thus, only the position of the wall and not its slope was determined by the radial distance of the

roller assembly from the center of the cam. Four pairs of roller assemblies were used to define each wavelength. The maximum, minimum, and two inflection points of each waveshape were set. It can be shown using the theory of elasticity that a series of such deflections about a straight line form a third degree curve which closely approximates a sine curve. Eight waves were set on the perimeter of the cam. The stationary wall was semicircular and therefore at any time there were four waves in the pumping section.

The fluid in the peristaltic annulus was contained in a tube attached to the moving and stationary walls. The tube was constructed from 1/16 inch Tygon sheet. A double faced adhesive tape was used to attach the tubing to the walls. After the tube was installed holes were cut through the tape and tube at the pressure ports. The stationary wall contained five ports positioned at intervals a quarter wavelength apart beginning two wavelengths from the upstream end of the pumping section. An overall view of the apparatus and a close-up view of the pumping section with the manifold used to connect the pressure ports to the transducer are shown in the photographs in Figure 6.

The tube was connected to reservoirs at both ends. An unaffixed length of tube accommodated the change of motion from the moving wall to the stationary reservoir connector. The first portion of the reservoir connection was a sleeve onto which the end of the tube was secured. The cross-section of the connector was oval within the sleeve section but changed to circular before the elbow. The elbow was connected to the main reservoir tank. Figure 7 shows the internal shape of the reservoir connector. The maximum height of the fluid in the reservoir

was controlled by an adjustable overflow weir. The upstream reservoir was continually fed to maintain a constant height of fluid. The height of the downstream reservoir was determined either by the height of the weir or by the maximum difference in head between reservoirs which could be supported by the pumping section. The heights of both reservoirs were monitored using manometers.

The accuracy of the machine depended on several items. The alignment of the axis of the cam and stationary outer wall was achieved by making the finishing cuts on the surface of the stationary wall with a cutting tool mounted in the bearings which supproted the cam. The distance between the staionary and moving walls was determined by the position of the roller assemblies which were adjusted with micrometer depth gauges attached to the stationary wall. Allowance was made for the thichkness of tape and tubing between the walls.

The value of "a" used in the experiments was 0.125 inch. The wavelength, λ = 12 inches, equals the stationary wall perimeter divided by half the number of wave shapes on the cam and yielded a/λ approximately 0.01. The ratio of a to R used to determine the accuracy of approximation of the linear geometry by an annular geometry was also approximately 0.01. The aspect ratio, a/w, which determines the accuracy of the two dimensional assumption, varied because of the constant perimeter of the tube. As the tube was squeezed, the wall which formerly was part of the end became a part of the side wall (See Fig. 5). The smallest ratio of a/w for ϕ = 0.5 was 0.1.

The cam was driven with a variable speed motor which provided a range of wave speeds, c, from 2 cm/s to 30 cm/s. A water soluble oil,

Ucon, was chosen for the operating fluid so that a range of viscosities could be obtained. The pressure-time data reported in Fig. 11 were taken with a wave speed, c, equal to 3.4 cm/s and a viscosity of 126 centipoise.

Apparatus Number Two. The following is relevant to the apparatus on which the effect of increasing Reynolds number was measured. A cross-section of the pumping section is shown in Figure 8. The moving wall was made of a band of spring steel with a rubber sheet attached to it. The seal on the top and bottom walls of the channel was made by the rubber sheet. The shape of the moving wall was controlled by rollers which were mounted on the cam. The moving wall can be described as a circle with perturbations on its periphery. At the perturbations projecting outward, aluminum rollers were used to impose the constricted regions of the flow channel. Magnetic rollers pulled on the wall to impose inward perturbations, i.e., the expanded regions of the flow channel. Each wavelength had 8 rollers of which 3 were magnetic. The pressure exerted by the fluid in the reservoirs acted to push the moving wall against all the rollers. The cam had 6 wave shapes about its perimeter. At any time three of these wavelengths were in the region of the stationary wall.

Bending the rubber sheet into a three dimensional curve caused a restoring force in the rubber. This force pressed the edge of the sheet against the top and bottom of the channel to seal the fluid in the channel. The seal at the top is curved away from the stationary wall to give an unobstructed view of the flow field for visual studies: the machine was constructed by Weinberg for that purpose[8]. Figure 9

illustrates the manner in which the reservoir connections were made. The rubber sheet is continuous onto a steel flap and also acts as a seal in this region. The flap allows for the transition between the peristaltic motion and the solid connection at the reservoir: its motion is that of half a standing wave. The reservoirs are positioned vertically above the offset space opposite the flap. Fluid height in the reservoirs was controlled by variable height overflow weirs. The upstream reservoir was constantly over-supplied with fluid so that the fluid height would always be that of the overflow weir. The downstream reservoir was supplied by the pumping action of the peristaltic section. The height of each reservoir was measured with a manometer.

The alignment of axes of the stationary wall and cam was done by positioning the stationary wall relative to the cam and then permanently affixing it. The gap between walls was set using a micrometer. The micrometer was zeroed from a set of rollers which were adjusted to touch the stationary wall. The value of "a" used for the experiments was 0.65 cm. Geometric ratios for the experiment were $a/\lambda = 0.01$, $a/R = 0.01$, and $a/w = 0.03$.

The Reynolds number was varied by changing the wave speed and/or the viscosity. The variable speed drive produced wave speed, c, between 2 and 35 centimeters per second. The viscosity of the fluid was selected by the proportions of glycerine and water used in the mixture. The range of viscosities was from 1 to 250 centipoise.

Two photographs of apparatus number two appear in Figures 10a and 10b.

Experimental Measurements

The measurement of time-mean flow involved collecting fluid from the overflow weir in the downstream reservoir during a measured time and then measuring the volume of the collection. The time-mean flow is given by dividing the volume of the collection by the time span of the collection. Because the flow is unsteady, a large enough volume must be collected so that stopping the collection at different times causes no appreciable deviation between measurements. Each collection consisted of the volume carried by at least 6 waves. Multiple measurements of time-mean flow for the same viscosity, wave speed, and pressure rise showed that by using 6 waves the values of $\overline{Q}$ would differ by no more than ±3 percent.

The pressure rise per wavelength was measured indirectly. The levels of the reservoirs were measured with manometers set to a common zero level. The difference in height between the reservoirs was divided by the number of waves in the pumping section to give the pressure rise per wavelength. This method has two difficulties. First, it assumes the number of waves in the channel is equal to the number of waves with velocity profiles caused only by the peristaltic walls. This is untrue because of end effects near the reservoirs; the fluid entering from a reservoir has a slug-flow type of velocity profile. The length required for the velocity profiles to develop is a function of Reynolds number. An estimate of the developing length can be made using the growth of a flat-plate boundary layer as a model of the change in velocity profile in the region of the reservoir and peristaltic channel. If the peristaltic walls are considered to be the only

influence on the velocity profiles when the boundary layer has reached a height equal to the mean half height, a, the developing length, d, extending from the reservoir into the channel is

$$\frac{d}{\lambda} = 0.04 \frac{a^2 c}{\lambda \nu} = 0.04 \text{ Rey.} \qquad \text{Eq. 13}$$

Equation 13 was obtained by rearranging an approximate relationship between the height of a boundary layer at some distance from the edge of a flat plate and the Reynolds number based on the distance from the edge[9]. For a Reynolds number of 8 the developing length is 10 percent of the number of wavelengths, 3, in the pumping section of apparatus number two. The second difficulty occurred for large geometric ratios, i.e., $\phi > 0.6$. For this case the flow carried by a wave was sufficient to cause a significant fluctuation in the heights of the reservoirs. The fluctuations were caused by the overflow characteristics of the weirs and the limited cross-sectional area of the reservoirs. Maximum and minimum reservoir heights were measured and used to determine band limits about average values of ΔP_λ.

Measurements of pressure versus time were taken with a variable-capacitance, differential-pressure transducer connected to a time-base recorder. All the pressure measurements were taken with respect to a pressure port two wavelengths from the beginning of the peristaltic section. The pressure manifold used to connect the ports to the transducer is seen in Figure 6. On the recorder an event marker was activated by a microswitch which was triggered by projections at a fixed point on each wavelength. These signals were used to establish the

origin of the time base for the pressure pulses. The signals in conjunction with the chart speed of the recorder were used to determine the wave speed.

Viscosity, the remaining variable quantity, was measured either with a Saybolt viscometer or a Brookfield viscometer. Agreement between viscometers when their ranges overlapped was within 2%.

Results and Conclusions

Apparatus Number One. The experimental measurements of pressure versus time are presented graphically in Figure 11. Figure 12 is a corresponding graph of ΔP_λ versus $\overline{Q}$. The measurements for the graphs in both figures were carried out on the apparatus of Figs. 5 and 6 with a tubular peristaltic channel; the amplitude ratio, ϕ, was 0.5. All the measurements for these two figures were done with the same viscosity and wave speed: the Reynolds number was 0.009. In Figure 11 there is an apparent discrepancy between the two-dimensional theory (dot-dash curves) and the experimental measurements (dashed curves). The experimental pressure traces lag the theoretical ones in time and have approximately 20 percent smaller magnitudes.

A close examination of the experimental apparatus showed that the peristaltic section did not really end in constant-pressure reservoirs. Rather, the sleeve section of the reservoir connection acted as a resistance between the reservoir and the peristaltic channel. If the resistance of these end sleeves is characterized by

$$P_R - P' = kQ \qquad \text{Eq. 14}$$

then a modified theory to take these resistances into account results in pressure-time curves more similar to the experimental curves. (A derivation of the equations describing these curves is presented in Appendix 1.) The solid curves shown in Figure 11 are calculated for a non-dimensional value of $R = k4\pi a^3/3\mu\lambda = 8$ evaluated as described in App. 2 from the dimensions of the reservoir connection. Despite the slightly better agreement of the experimental and the resistance-model

pressure traces with regard to shape, the time lag and magnitude difference between the traces are still present.

The capacitance of the transition section in the reservoir connection is another probable cause of this time lag. At each connection a length of tube was left unattached to accommodate the change of motion from the peristaltic moving wall to the stationary reservoir connection. Since peristaltic motion was imposed on only one wall of the tube this length had a relatively inactive side. This inactive side was easily seen while the apparatus was running. It always bulged radially outwards due to the pressure imposed by the fluid in the reservoir, but the amount of bulge changed as different parts of the wave moved past it. This effect was judged to be too complex to be added to the model of the experiment.

As predicted by the low-Reynolds-number theory, the experimental points of ΔP_λ versus $\bar{Q}$ fall near a straight line in Fig. 12. The intercepts are the interesting information. An effective width of two-dimensional channel is necessary to relate $\bar{Q}$ to Θ according to the relationship $\bar{Q} = \Theta(bcw)$. This width is indeterminate in two ways. First, there are the rounded end walls which affect the flow near them. The aspect ratio provides an indication of the importance of the end walls relative to the two-dimensional flow and therefore an indication of the effective two-dimensional width. In apparatus number two the end walls decreased Θ_{max} by 5 percent. Since apparatus number one has a three times larger aspect ratio than apparatus number two, a 10 - 15 percent decrease in Θ_{max} might be expected. Second, because the flow is contained in a tube of constant

perimeter, the width changes inversely as the distance, h, between the side walls. This is illustrated in Figure 5.

Instead of assuming some width and then comparing the theoretical and experimental time net flows, a width, w, is calculated tc make the theoretical and experimental flows equal. A theoretical value of the non-dimensional time-mean flow can be calculated for the model of the apparatus with and without resistance at the ends of the peristaltic length. Using the value of resistance characteristic of the dimensions of the reservoir connections, the width of two dimensional channel is 6.8 cm; for no resistance the width is 6.0 cm. For comparison, the distance between ends of the tube assuming that the ends are semi-circular and the channel height is 2a is 7.5 cm. Considering only the retarding effect of the end walls as estimated by the aspect ratio the width of 7.5 cm would change to 6.4 to 6.8 cm of effective two-dimensional width. The choice between models of the experiment used to give a value of Θ_{max} seems to be an arbitrary one.

The addition of end resistances to the two-dimensional model of the experiment does not change the value of $\Delta P_{\lambda max}$. The experimental intercept is 25 percent low; this discrepancy might be attributed to two sources. The first source is the rounded ends of the tube which have a retarding effect on the flow near them. The flat end-walls of apparatus number two reduced its $\Delta P_{\lambda max}$ by approximately 2 percent. (This is described on page 28 and can be determined from Figure 13a). The aspect ratio of apparatus number one is three times larger than that of apparatus number two; therefore a larger percentage reduction in $\Delta P_{\lambda max}$ for apparatus number one would be expected. Because the

perimeter of the tube was constant in length the rounded ends underwent a peristaltic motion 180 degrees out of phase with the major peristaltic motion. This secondary peristalsis had a small amplitude ratio, ϕ, since its "a" was half the width, w. The pressure gradient of this secondary peristalsis is imposed by the major peristaltic channel. Since $\Delta P_{\lambda max}$ is a strong function of ϕ, the secondary peristalsis is operating at a ΔP_{λ} greater than its $\Delta P_{\lambda max}$ and therefore has a negative time-mean flow. Thus, this secondary peristalsis at the ends of the tube acts as a leakage path upstream, whose flow, when algebraically summed with the flow in the major peristaltic channel, allows the experimental time-mean flow to be zero at a lower experimental $\Delta P_{\lambda max}$. The complex nature of the flow occurring in the reservoir connections might be another source of the ΔP_{λ} discrepancy.

With the above results the two-dimensional theory cannot be definitely declared correct, but the fault may lie with the experimental ambiguities cited above. The results of experiments by Weinberg on the three wavelength, no tube apparatus, here labelled apparatus number two, have demonstrated the validity of the pressure-time curves and the ΔP_{λ} - Θ graph[10]. Because of the uncertainties in the above results, and the misfortune of a broken drive train in the apparatus, it was decided to perform the further studies of Reynolds number effect on the three wavelength apparatus, i.e., apparatus number two.

Apparatus Number Two. The following section reports the changes in ΔP_{λ} and Θ due to non-zero Reynolds number: these experimental results are the only ones of significance. Graphs of ΔP_{λ} versus Θ at various Reynolds numbers appear in Figures 13a, 13b, 13c, 13d, and 13e.

These data were taken on the three wavelength machine with the amplitude ratio, ϕ, set at 0.7. The actual width, w = 9.5 inches, was used to convert experimental measurements of $\overline{Q}$ to Q. On each graph are plotted three theoretical curves which represent different zero-Reynolds-number models of the experimental apparatus. The two-dimensional curve (solid line) is a plot of Equation 8; this curve does not account for any end-wall effects. The retarding effects of the end walls have been taken into account in the curve labelled two-dimensional, rectangular channel (dot-dash line). This curve was obtained numerically using a technique in which each wavelength was broken into small segments with individual aspect ratios determined by the local height, h. The relationship between pressure gradient and flow for each segment was obtained from an approximate solution for flow in a retangular channel. The curve labelled two-dimensional, rectangular channel with leakage path (dashed line) is fit to the low-Reynolds-number data. This model of the experiment assumes fluid leaks upstream in the region near the upper seal where the height between peristaltic walls is larger than 2h; this region is marked "A" in Figure 8. The leakage flow in this path is modelled as a Poiseuille flow with the same pressure gradient as that in the two-dimensional, retangular channel. The area of the leakage path, which was chosen to fit the low-Reynolds-number data, corresponds to a circular area of 0.5 cm^2.[11] This area is about 30% less than the "extra" area caused by the shape of the upper seal; this would be expected due to the difference in geometries. Fluctuations in the heights of the reservoirs occurred because of the large, unsteady flows associated with the large amplitude ratio, ϕ. The maximum and minimum values of ΔP_λ

caused by these fluctuations are shown as band limits in Figs. 13a, 13b, 13c, 13d, and 13e. Since the flow which causes the fluctuations is unsteady, the limits are instantaneous values of ΔP_λ. The value of ΔP_λ obtained from a numerical average of the maximum and minimum heights in each reservoir (solid points) is probably a time-average value because of the progressive-wave motion in which the fluctuations originate.

From the graphs of Figures 13a, 13b, 13c, 13d, and 13e two summary graphs may be constructed; they are the graphs of the experimental intercepts, $\Delta P_{\lambda max}$ and Θ_{max}, versus Reynolds number. These are shown in Figures 14 and 15. The solid curve appearing in these graphs is Jaffrin's prediction of the effect of Reynolds number[12]. The short dashed line is the value of the intercept of the curve in Figure 13 for a two-dimensional, rectangular channel with leakage.

The band limits on the graph of Θ_{max} versus Reynolds number represent the limits of confidence in the experimental measurements. To obtain the band limits on each Θ_{max} - Rey point, the graph of ΔP_λ vs. Θ for that Reynolds number had two lines drawn on it. The lines are drawn through the outer data points so all other data points were enclosed within the lines. The limits on Θ_{max} are the intercepts of the envelope lines with the Θ-axis. For cases where a data point did not lie on the Θ-axis a maximum Θ value was obtained from a best straight line drawn through the data points. These techniques are illustrated in graphs in Figs. 16a, 16b, and 16c. The band limits on $\Delta P_{\lambda max}$ are the same type which appear on Figs. 13a, 13b, 13c, 13d, and 13e. No extrapolation was necessary for the maximum pressure rise per wavelength

since the experimental technique was to raise the weir so no overflow could occur. This may be contrasted to the measurement of Θ_{max} where the overflows must be set to an equal height and where the fluctuation of the upstream and downstream reservoirs can differ. The greater ease and lesser possibility for error may account for the closer adherence of the ΔP_λ data points to the theoretical prediction. This closer adherence for high Reynolds number may be specious since the last two points shown have considerable lengths of the peristaltic channel where velocities are partially influenced by the reservoir. The lengths as estimated by Equation 13 are 0.7 and 1.2 wavelengths, respectively.

The extremely small pressure rise which occurs for small ϕ and intermediate Reynolds number prevented experimental verification of the decrease in $\Delta P_{\lambda max}$ as predicted by Jaffrin's solution. A zero-Reynolds-number theory calculation showed the maximum pressure rise for $\phi = 0.4$ and Rey = 1 to be 4 mm of water. Because of the reservoirs any measurement of so small a pressure rise would have been spurious. With such a small maximum pressure rise a large error would be present in setting the overflow weirs for $\Delta P_\lambda = 0$; therefore no measurements of Θ_{max} versus Reynolds number were attempted for small ϕ.

The experiments on the effect of increasing Reynolds number are useful in two ways. First, they show the correct nature of the expansion solution. There is no appreciable deviation from the low Reynolds theory until a Reynolds number of 1. Second, they give a limit to the application of the expansion. The experimental results

still correlate well at a Reynolds number of 10. This can be compared with the value of 3 where the difference between Θ_{max}/ϕ^2 predicted by the two-dimensional, zero-Reynolds-number theory and Θ_{max}/ϕ^2 predicted by Hanin's solution for small ϕ is equal in magnitude to the difference between Θ_{max}/ϕ^2 predicted by Jaffrin's solution and Θ_{max}/ϕ^2 predicted by Hanin's solution.

References

1. Shapiro, A. H., Jaffrin, M. Y., Weinberg, S. L., "Peristaltic Pumping with Long Wave Lengths at Low Reynolds Number", in J. Fluid Mech. (1969), vol. 37, part 4, pp. 799-825.
2. Jaffrin, M. Y., "Inertia and Streamline Curvature Effects on Peristaltic Pumping", unpublished manuscript, Fluid Mechanics Laboratory, Department of Mechanical Engineering, Massachusetts Institute of Technology.
3. Latham, T. W., "Fluid Motions in a Peristaltic Pump", S. M. Thesis, Massachusetts Institute of Technology
4. Shapiro, A. H., op. cit.
5. ibid.
6. Weinberg, S. L., "Theoretical and Experimental Treatment of Peristaltic Pumping", Sc. D. Thesis, Massachusetts Institute of Technology, to be presented February, 1970.
7. Jaffrin, M. Y., op. cit.
8. Weinberg, S. L., op. cit.
9. Schlichting, H. (transl. by Kestin, J.), Boundary-Layer Theory, 6th Ed., p. 26, McGraw-Hill Book Co., New York (1968).
10. Weinberg, S. L., op. cit.
11. ibid.
12. Jaffrin, M. Y., op. cit.

Appendix 1

The experiment may be modelled as a combination of two Poiseuille resistances, two constant pressure reservoirs, and a two-dimensional, zero-Reynolds-number peristaltic length of four wavelengths. These elements are connected as shown in Figure A1.

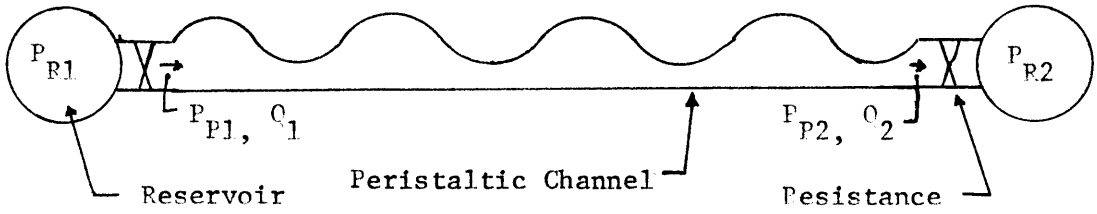

Figure A1

The various parts of the model are characterized by the following relationships:

$$P_{R1} = \text{given constant} \qquad \text{Eq. 1a}$$

$$P_{R1} - P_{P1} = kQ_1(t) \qquad \text{Eq. 2a}$$

$$\frac{\partial Q}{\partial X} + \frac{\partial h}{\partial t} = 0 \quad \text{in the peristaltic channel} \qquad \text{Eq. 3a}$$

$$Q = -\frac{h^3}{3\mu}\frac{\partial P}{\partial X} \quad \text{in the peristaltic channel} \qquad \text{Eq. 4a}$$

$$P_{P2} - P_{R2} = kQ_2(t) \qquad \text{Eq. 5a}$$

$$P_{R2} = \text{given constant} \qquad \text{Eq. 6a}$$

Boundary conditions over the peristaltic length are

$$\text{at } X = 0 \quad P = P_{P1}, \qquad Q(0,t) = Q_1(t) \qquad \text{Eq. 7a}$$

$$\text{at } X = L \quad P = P_{P2}, \qquad Q(4\ ,t) = Q_2(t) \qquad \text{Eq. 8a}$$

The wall is described by a sine function, namely

$$h = a + b \sin \frac{2\pi}{\lambda} (X-ct) \qquad \text{Eq. 9a}$$

Since the peristaltic wall shape is a function of X-ct the continuity equation, Eq. 3a, can be integrated to give

$$Q = ch + f(t) \qquad \text{Eq. 10a}$$

The momentum equaiton, Eq. 4a, with Q substituted from above, is rearranged and integrated between the ends of the peristaltic channel at constant time to give

$$P_{P1} - P_{P2} = \int_0^L \frac{3\mu c}{h^2}\, dx + \int_0^L \frac{3\mu}{h^3}\, f(t)\, dx \quad , \qquad \text{Eq. 11a}$$

Since time is constant it is possible to change the variable of integration from X to $\theta = \frac{2\pi}{\lambda}(X-ct)$. Eq. 11a with θ as the variable of integration is

$$P_{P1} - P_{P2} = \int_{\theta 1}^{\theta 2} c\, K \frac{d}{h^2} + \int_{\theta 1}^{\theta 2} Kf(t) \frac{d}{h^3} \qquad \text{Eq. 12a}$$

where $\theta 1 = \frac{2\pi}{\lambda}(-ct)$, $\theta 2 = \frac{2\pi}{\lambda}(L-ct)$, and $K = \frac{3\mu\lambda}{2\pi}$. Eq. 12a is solved for

f(t): which is substituted into Eq. 10a to obtain

$$Q(X,t) = ch(\theta) + \frac{(P_{P1} - P_{P2}) - \int_{\theta 1}^{\theta 2} cK \frac{d\theta}{h^2}}{\int_{\theta 1}^{\theta 2} K \frac{d\theta}{h^3}} \qquad \text{Eq. 13a}$$

Equations 1a, 2a, 5a, 6a, and 13a form a set of five simultaneous equations in five unknowns since at each end the flow through the resistance must be equal to the flow of the peristaltic length. A relationship between $\bar{Q}$ and the reservoir pressures can be obtained by solving these equations and then time averaging the resulting relationship. It is

$$\frac{P_{R2} - P_{R1}}{\mu c \lambda / a^2} = 4\left[\frac{3}{2}\frac{\phi^2}{(1-\phi^2)^{5/2}}\right]\left[3 - \left(\frac{2+\phi^2}{\phi} + \frac{R(1-\phi^2)^{5/2}}{4\pi\phi}\right)\Theta\right] \qquad \text{Eq. 14a}$$

where $R = 4\pi k a^3/3\mu\lambda$. The relationship simplifies to Eq. 8 of the theoretical section if there is no resistance.

The function, f(t) may be obtained in terms of the reservoir pressures, P_{R1} and P_{R2}, by solving the five equations above for P_{P1} and P_{P2} and substituting these into Eq. 12a. When this form of f(t) is substituted into the integrated continuity equation, Eq. 10, then Eq. 4, the momentum equation, with Q from Eq. 10 has the following form:

$$-\frac{\partial P}{\partial X} = \frac{3\mu c}{h^2} + \frac{3\mu}{h^3}\left\{ \frac{2kc\int_{\theta 1}^{\theta 2}\frac{d\theta}{h^2}}{\int_{\theta 1}^{\theta 2}\frac{d\theta}{h^3}} - 2kch\,(\theta 1) + P_{R1} - P_{R2}\right\}\frac{1}{\left[2K + \int_{\theta 1}^{\theta 2}\frac{d\theta}{h^3}\right]}$$

$$-\frac{3\mu c}{h^3}\left\{\frac{\int_{\theta 1}^{\theta 2}\frac{d\theta}{h^2}}{\int_{\theta 1}^{\theta 2}\frac{d\theta}{h^3}}\right\} . \qquad \text{Eq. 15a}$$

This equation is integrated between P_1 at $X = 0$ and P_n at $X = X_n = (2 + n/4)\lambda$ where $0 \le n \le 4$. Then $P_{P1} - P_{R1}$ is subtracted to form $P_n - P_{R1}$:

$$P_n - P_{R1} = \int_{\theta 1}^{\theta n}\left[-\kappa c\frac{1}{\bar{h}^2} + \frac{\kappa c}{h^3}\left\{\frac{\int_{\theta 1}^{\theta 2}\frac{d\theta}{\bar{h}^2} + Rh(\theta 1)}{R + \int_{\theta 1}^{\theta 2}\frac{d\theta}{\bar{h}^3}}\right\} + \left(\frac{P_{R2} - P_{R1}}{\bar{h}^3}\right)\left(\frac{1}{R + \int_{\theta 1}^{\theta 2}\frac{d\theta}{\bar{h}^3}}\right)\right] d\theta$$

$$+ \frac{R}{R + \int_{\theta 1}^{\theta 2}\frac{d\theta}{\bar{h}^3}}\left\{\kappa c\int_{\theta 1}^{\theta 2}\frac{2d\theta}{\bar{h}^2} - \bar{h}(\theta 1)\left(\int_{\theta 1}^{\theta 2}\frac{d\theta}{\bar{h}^3}\right) + P_{R2} - P_{R1}\right\} \qquad \text{Eq. 16a}$$

where $\bar{h} = h/a$, $\kappa = \frac{3\mu\lambda}{2\pi a^2}$, and $\theta_n = \frac{2\pi}{\lambda}(X_n - ct)$. For the pressure traces of Fig. 11, Equation 16a was nondimensionalized with respect to $(P_{R2} - P_{R1})$ given by Eq. 14a. Then, the pressure differences between the points X_n

and the upstream reservoir for a sequence of times were calculated numerically. The curves of Fig. 11 are the loci of points equal to $(P_n - P_{R1})/(P_{R2} - P_{R1}) - (P_0 - P_{R1})/(P_{R2} - P_{R1})$, where n ranges from one to three.

Appendix 2

For Poiseuille flow through a length, L, of two-dimensional channel with parallel walls separated a distance 2d, the relationship between the flow through half the channel, Q, and the pressures at the ends is

$$Q = \frac{d^3}{3\mu L} (P_1 - P_2) \qquad \text{Eq. 1-A}$$

The direction of the flow, Q, is from station 1 to station 2. Comparsion of Eq. 1-A with the relationship used to characterize the resistance of the reservoir connections Eq. 2a shows that

$$k = \frac{3\mu L}{d^3} \quad . \qquad \text{Eq. 2-A}$$

The non-dimensional form of the resistance used in Appendix 1 is

$$R = \frac{4\pi k a^3}{3\mu\lambda} = 4\pi \frac{L}{\lambda} \frac{a^3}{d^3} \quad . \qquad \text{Eq. 3-A}$$

The relative dimensions of the reservoir connector were $L/\lambda = 1/3$ and a/d slightly greater than one; $R = 8$ was used for the pressure-time graphs of the resistance model.

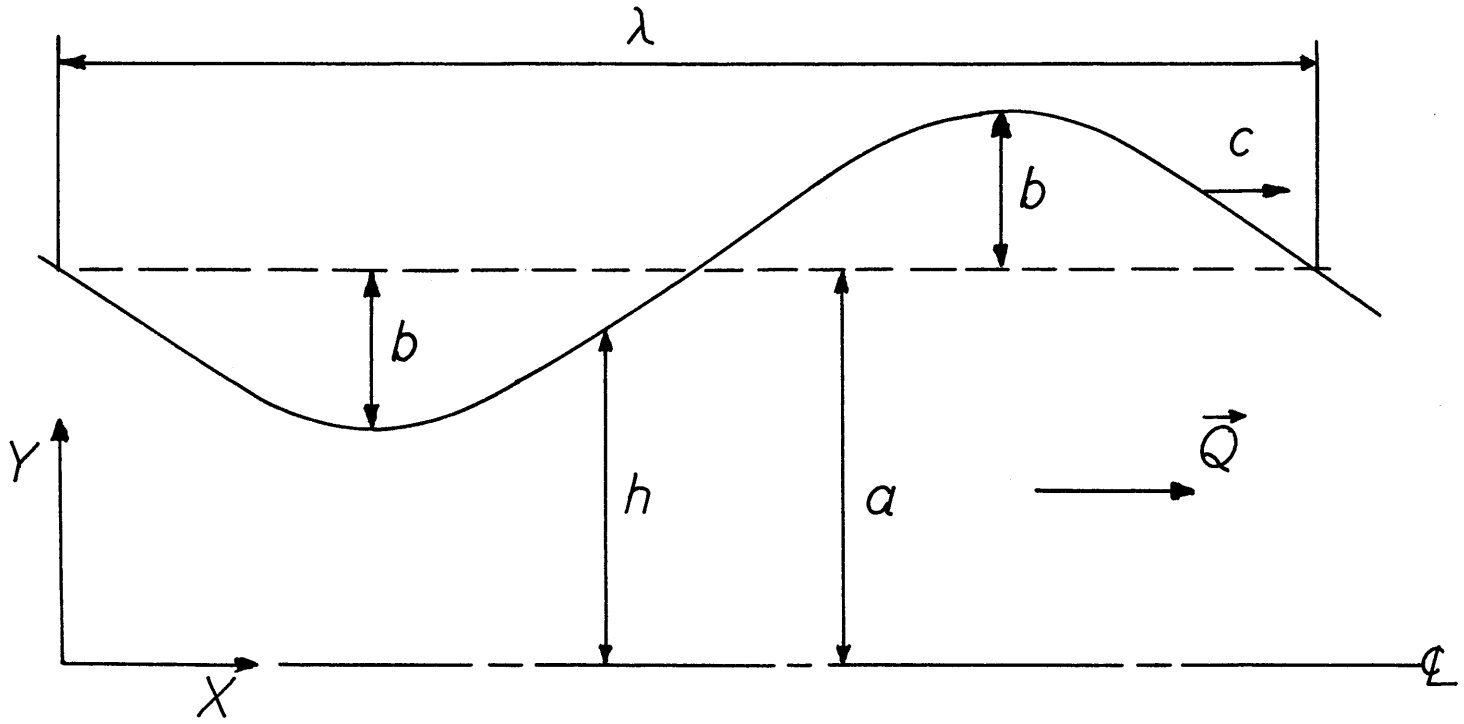

FIGURE 1 WAVE COORDINATES AND VARIABLES

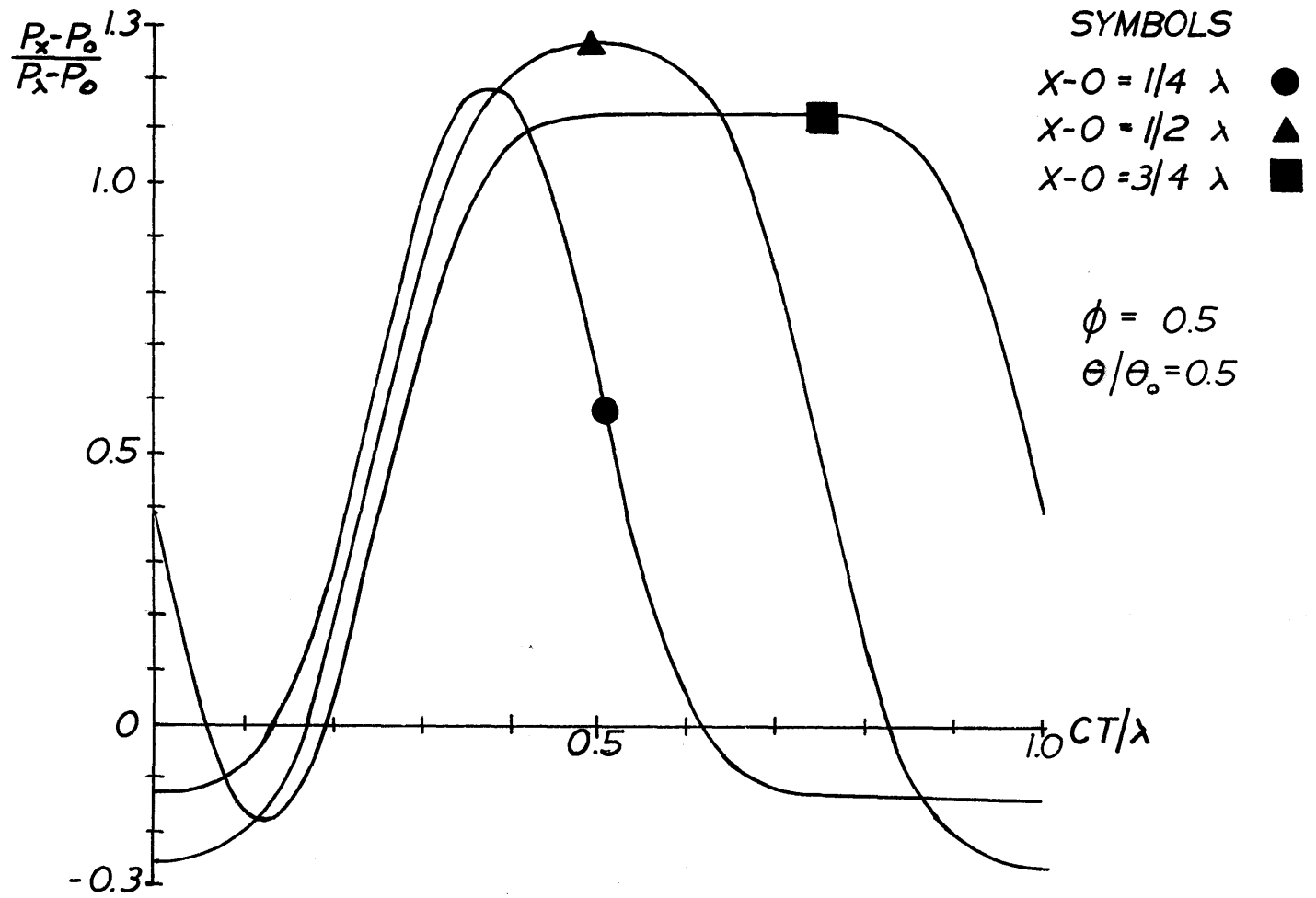

FIGURE 2

THEORETICAL PRESSURE-TIME CURVES

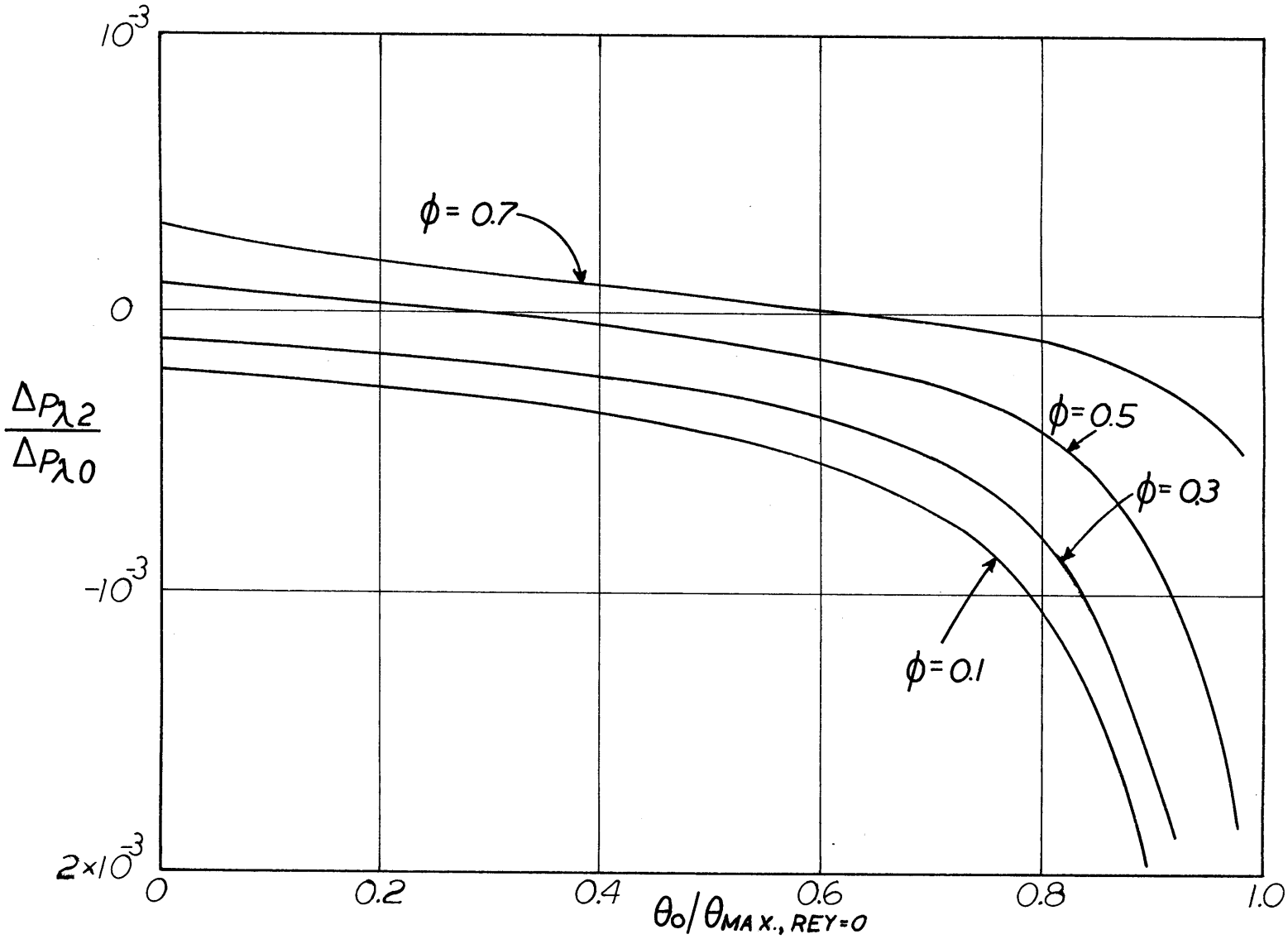
10^{-3}
0
-10^{-3}
2×10^{-3}
$\frac{\Delta P_{\lambda 2}}{\Delta P_{\lambda 0}}$
$\phi = 0.7$
$\phi = 0.5$
$\phi = 0.3$
$\phi = 0.1$
0
0.2
0.4
0.6
0.8
1.0
$\theta_0/\theta_{MAX., REY=0}$

FIGURE 3

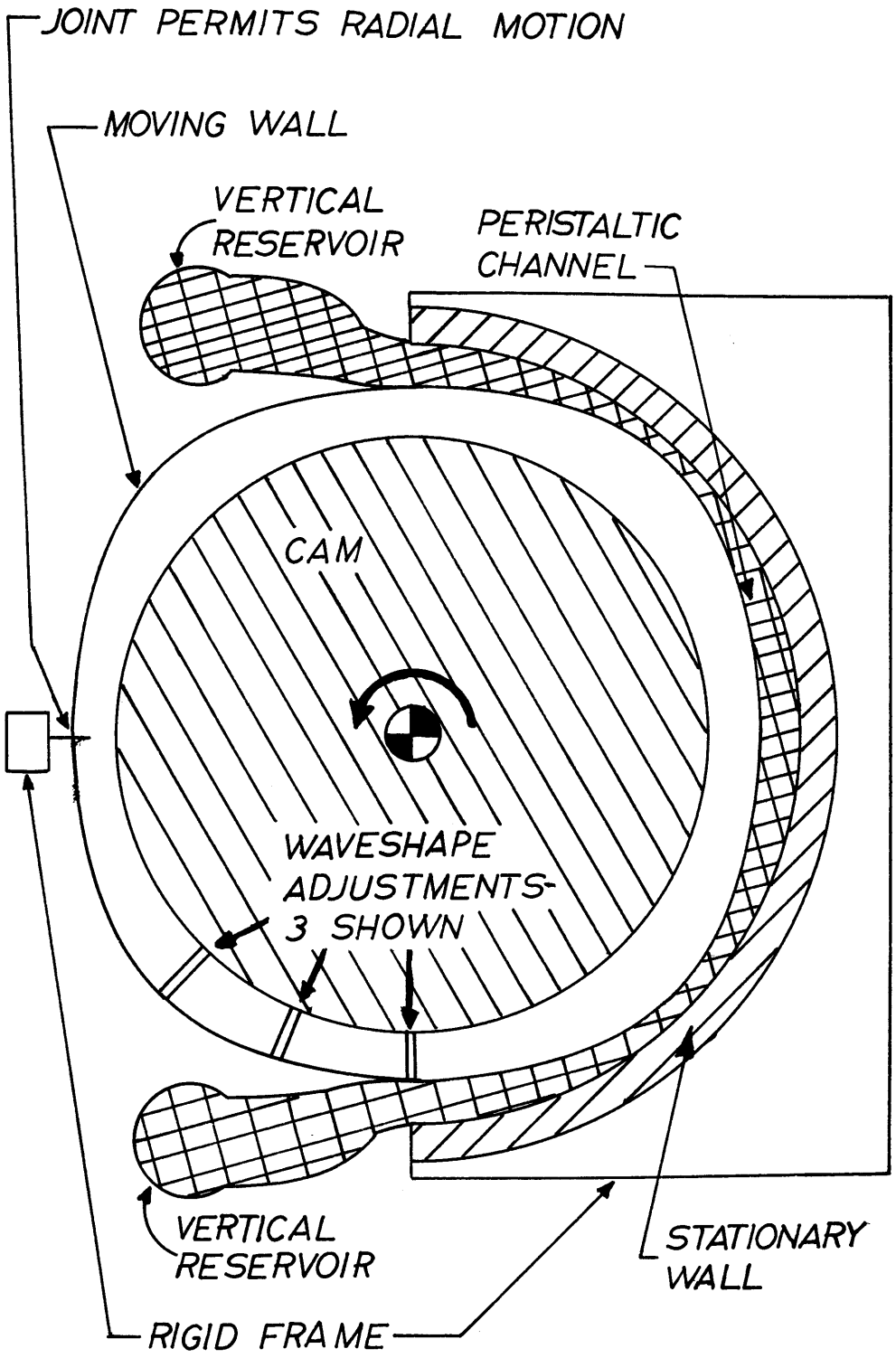

FIGURE 4 BASIC DESIGN OF THE EXPERIMENT

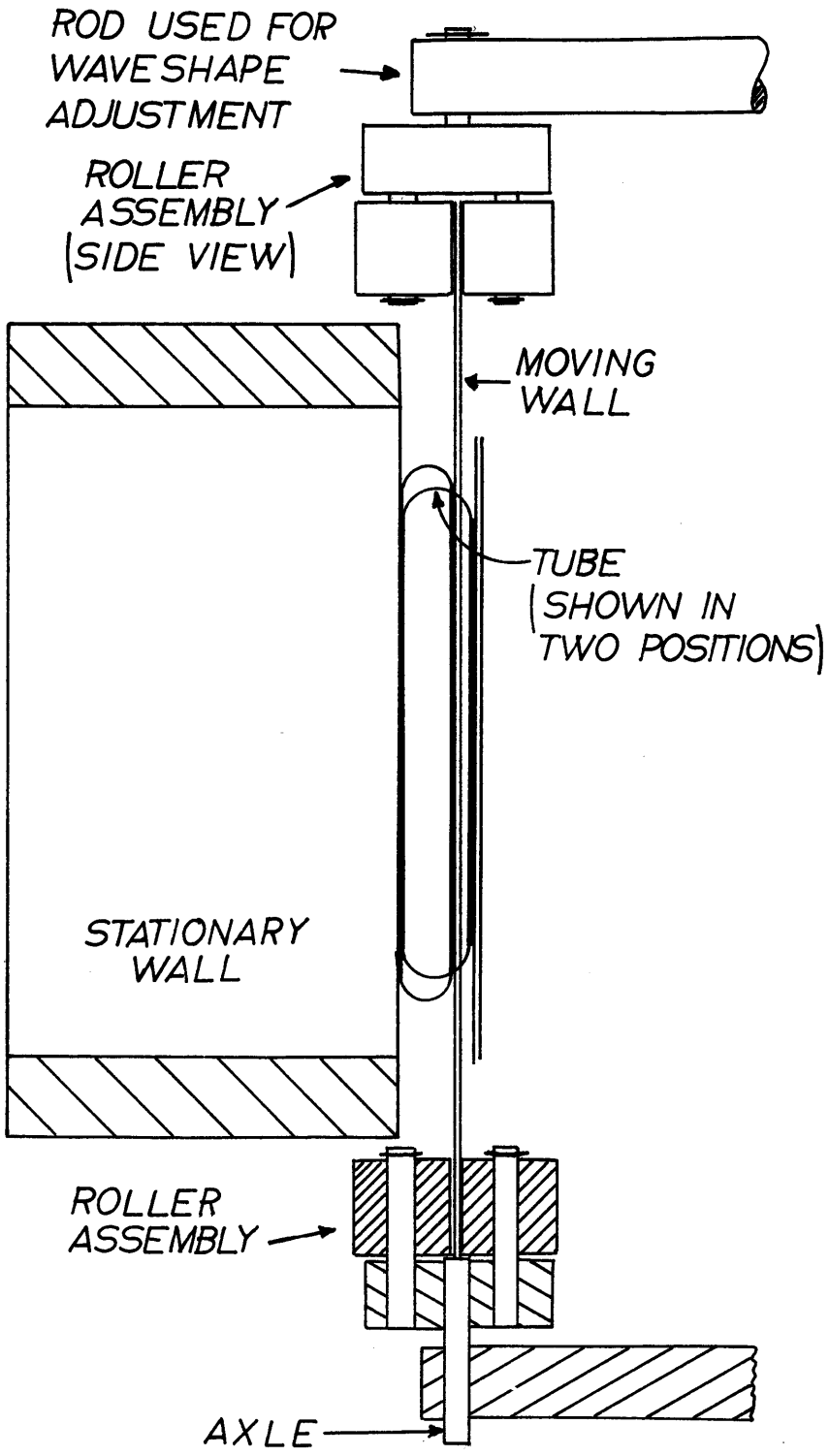

FIGURE 5 CROSS-SECTION OF PERISTALTIC CHANNEL

NO FIG. 6

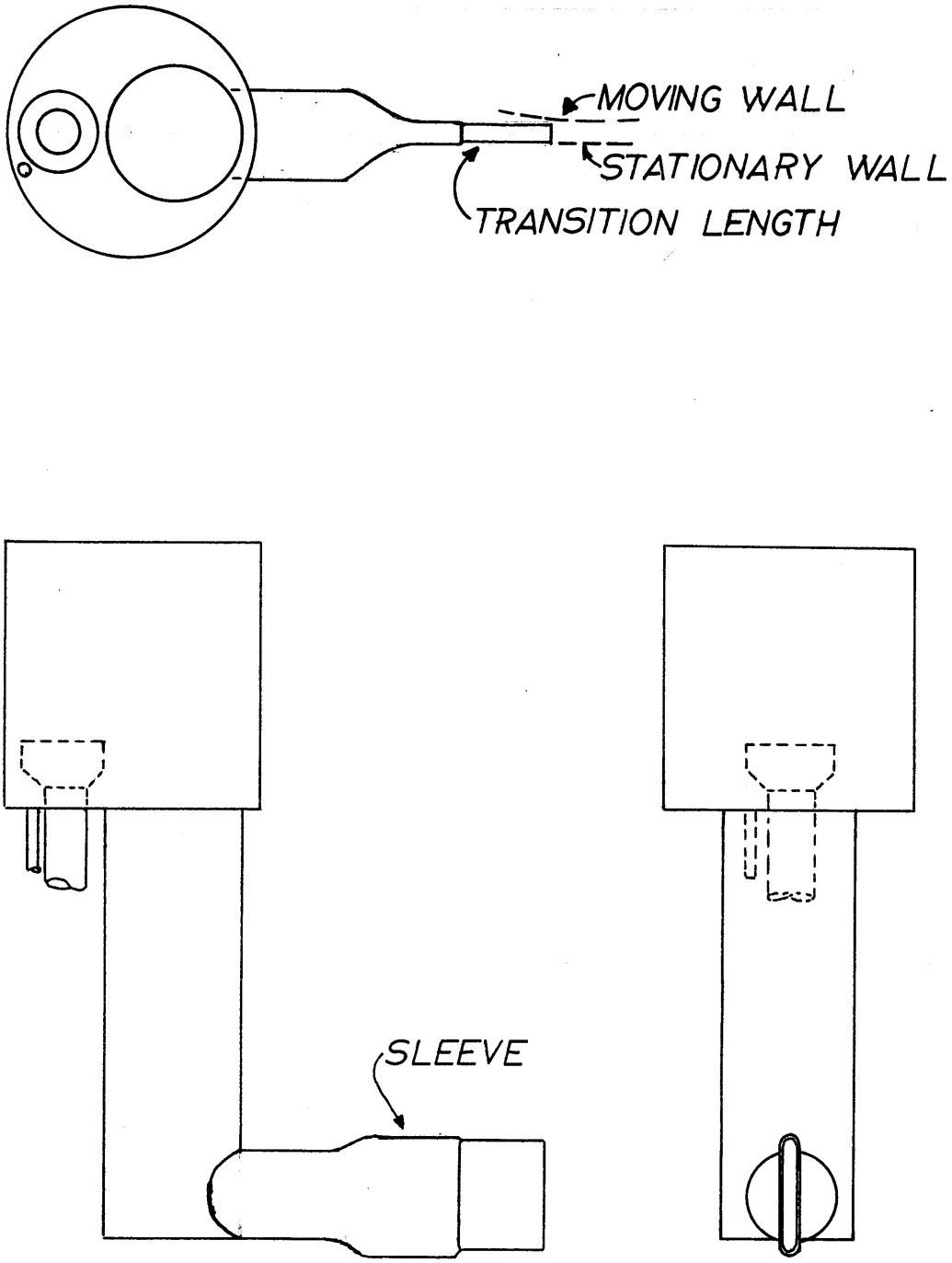

FIGURE 7 INTERNAL SHAPE OF RESERVOIR CONNECTOR

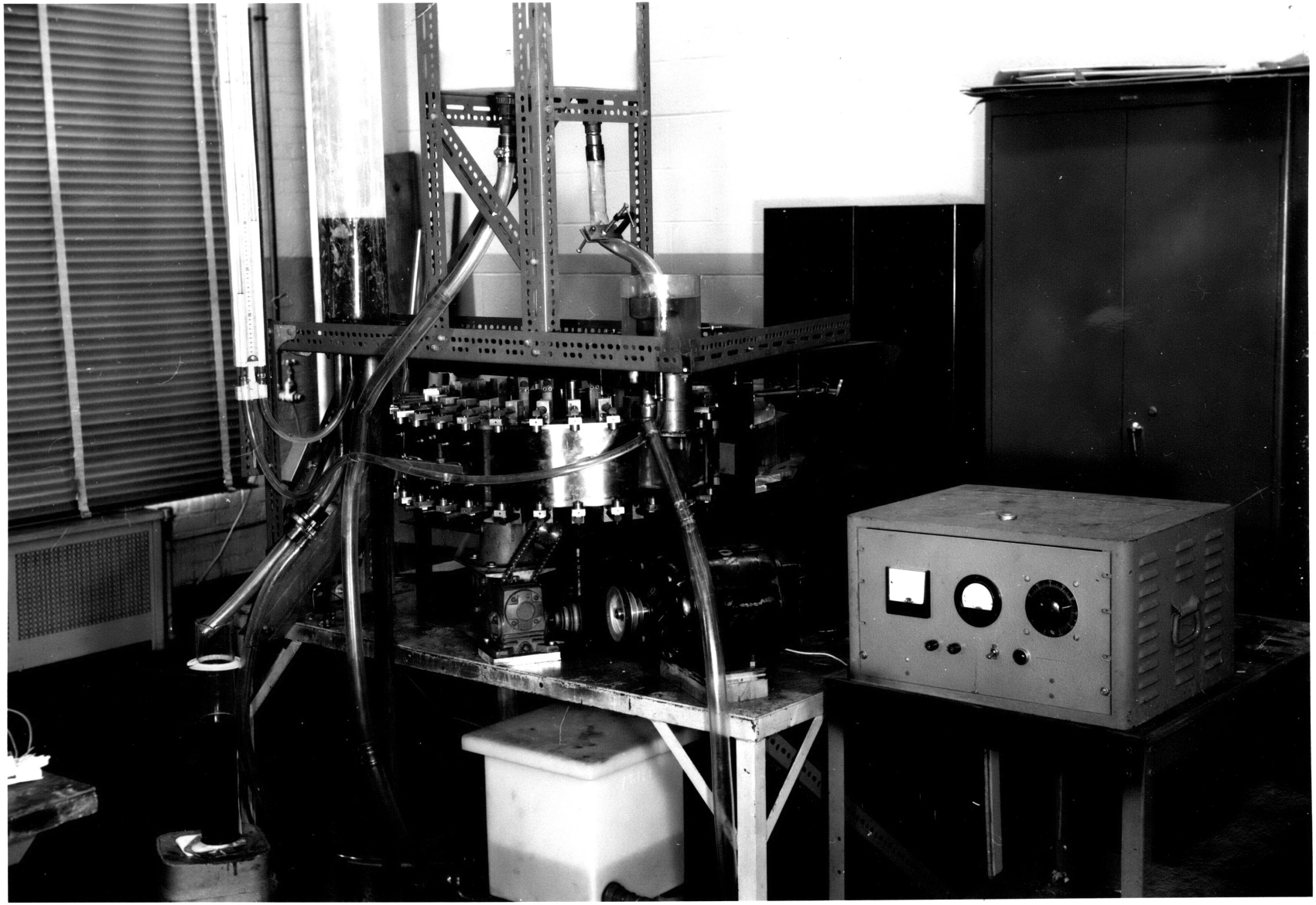

Figure 7a Overall View of Apparatus Number One

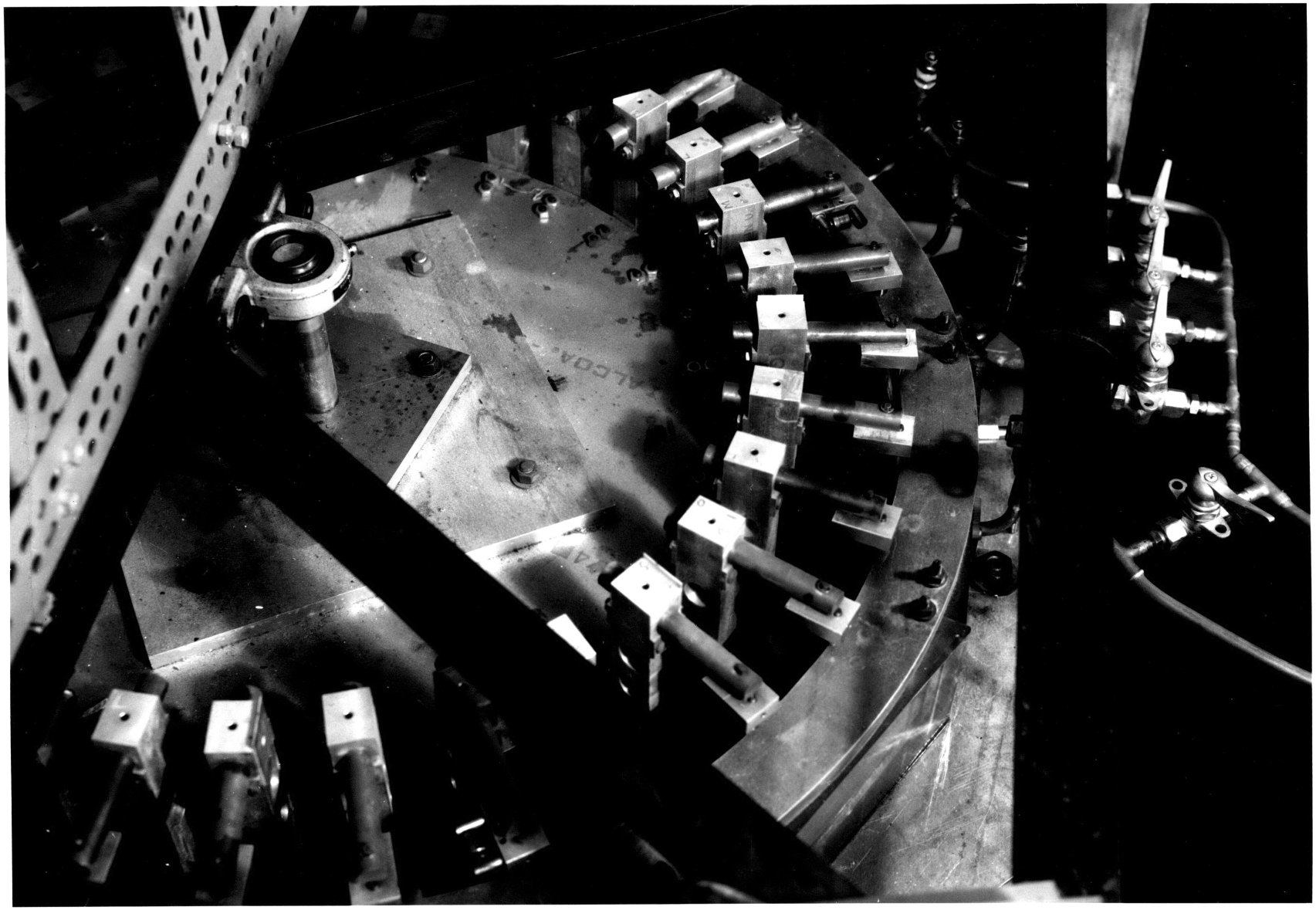

Figure 7b View of Peristaltic Section of Apparatus Number One

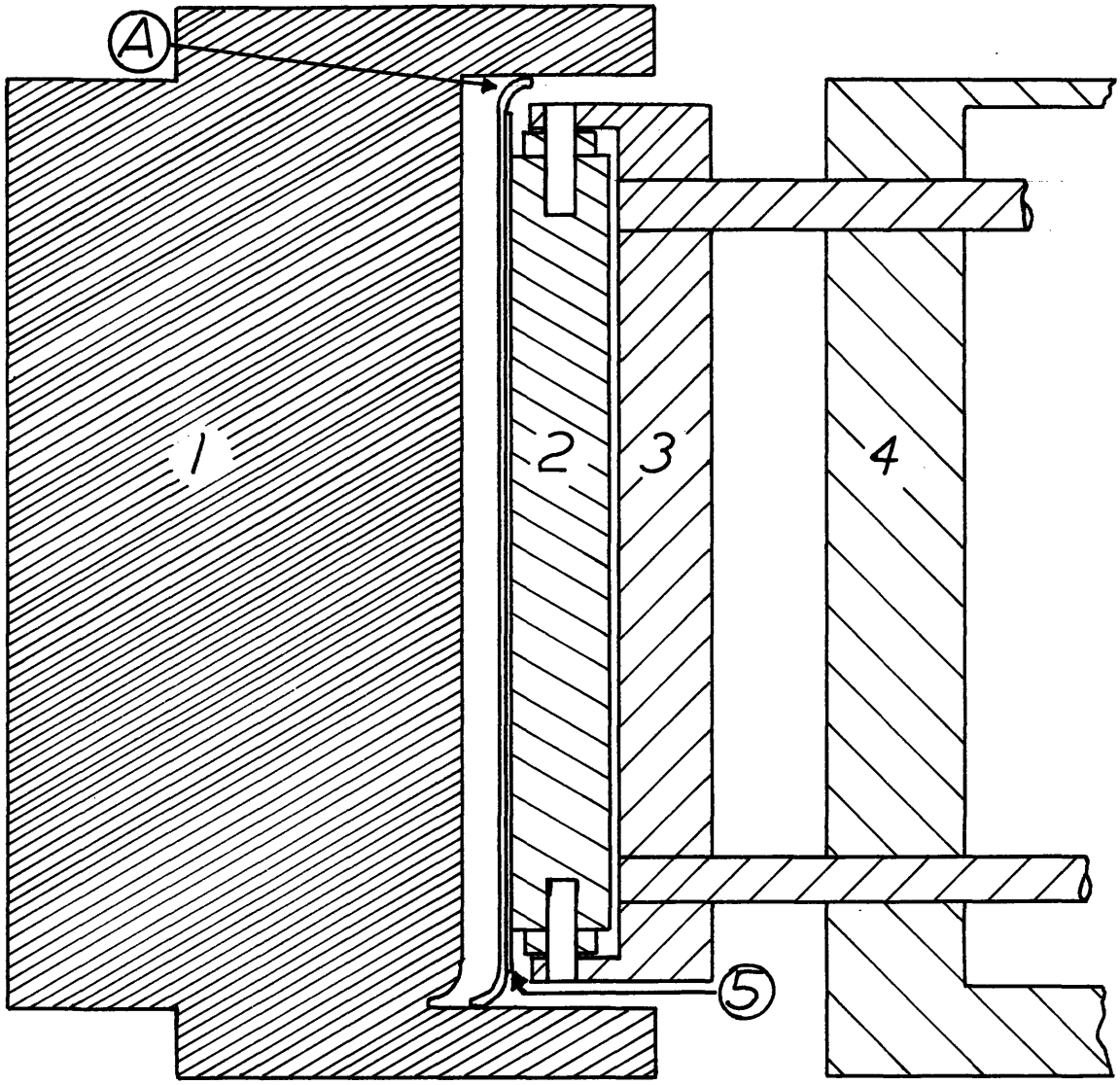

PART NO
1 STATIONARY WALL
2 ROLLER
3 RADIAL ADJUSTMENT
4 CAM
5 MOVING WALL

FIGURE 8
CROSS SECTION OF PUMPING CHANNEL

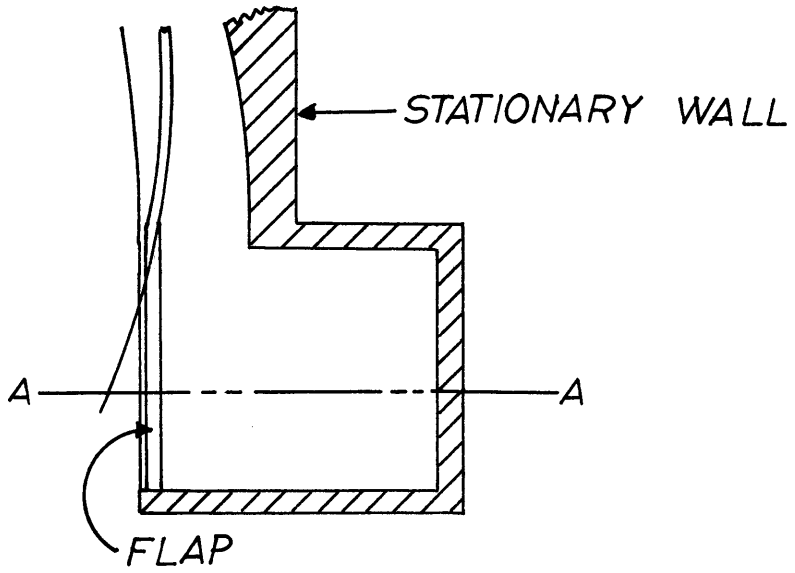

SECTION B-B

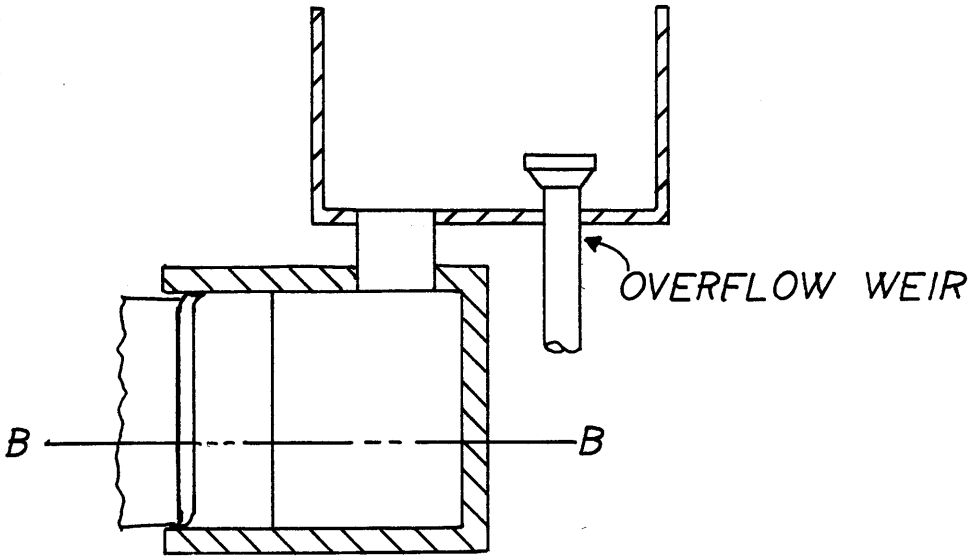

SECTION A-A

FIGURE 9 RESERVOIR CONNECTION

Figure 10a Overall View of Apparatus Number Two

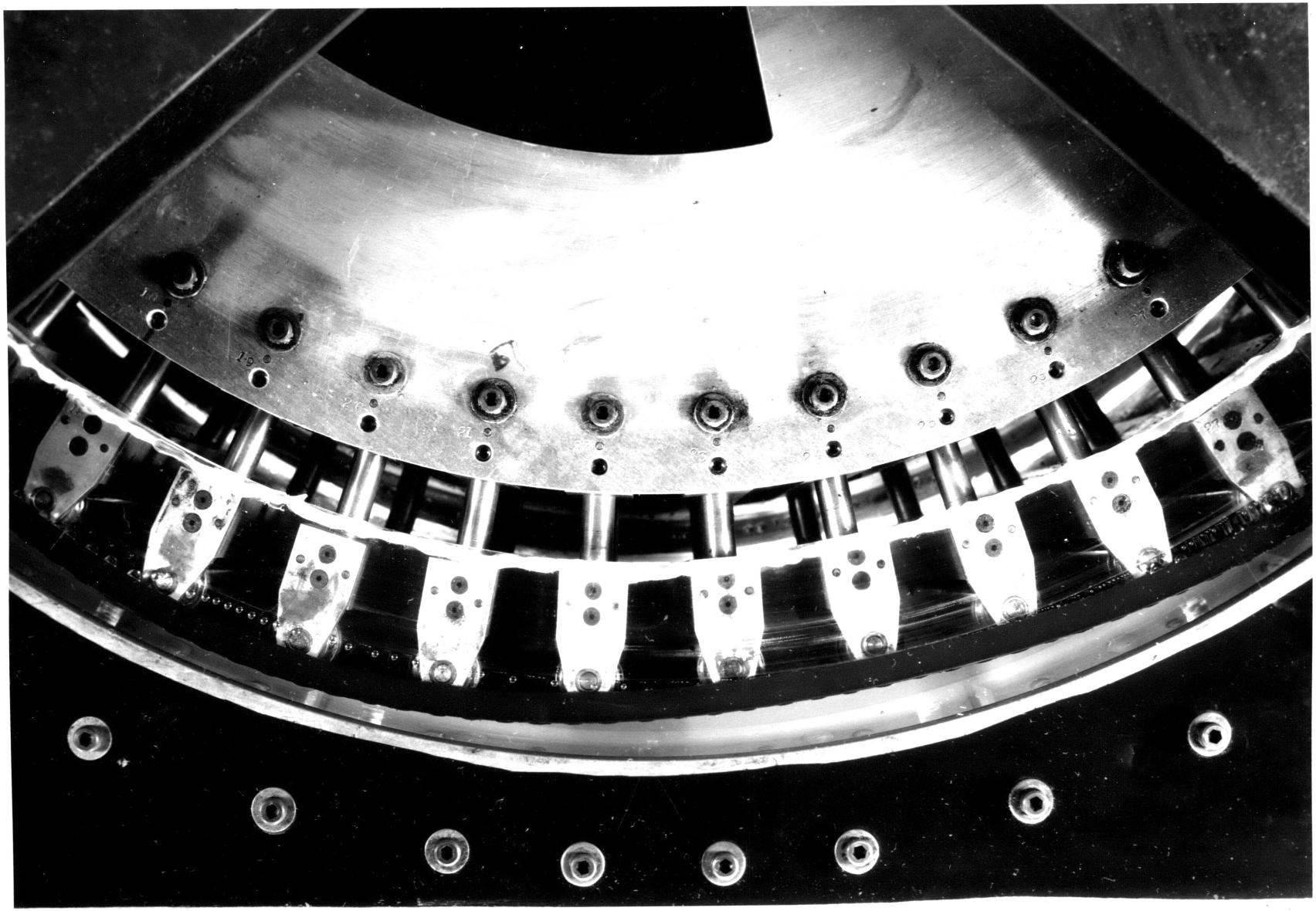

Figure 10b Top View of Peristaltic Channel in Apparatus Number Two

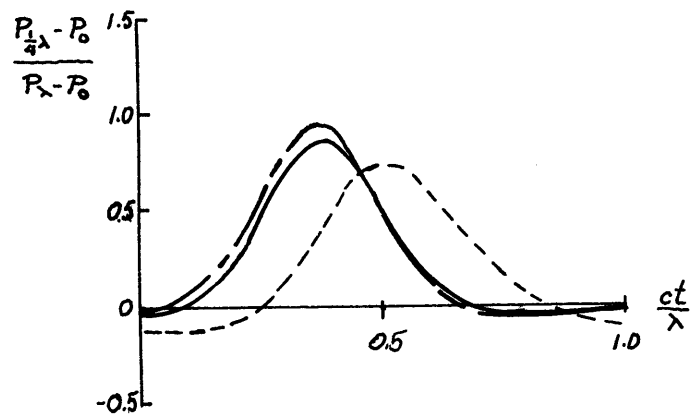

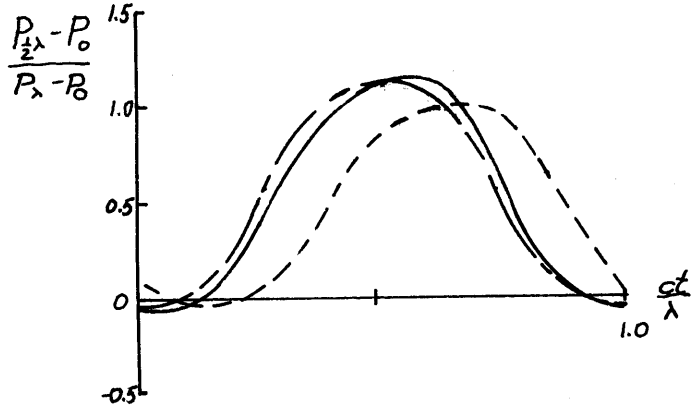

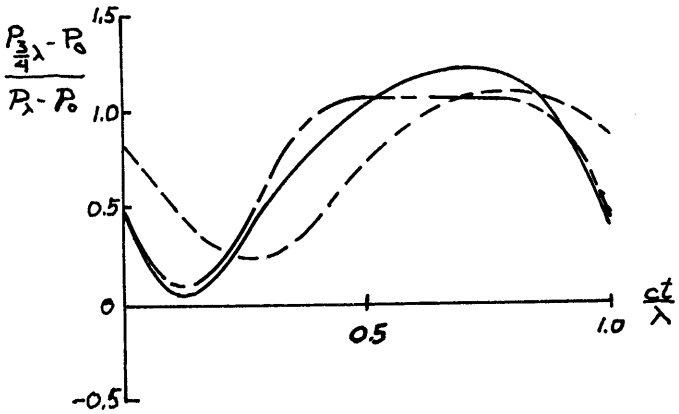

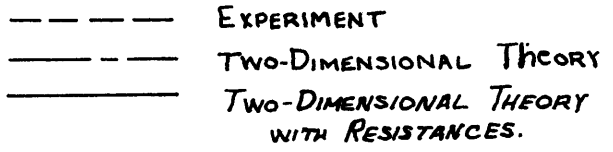

$\phi = 0.5 \quad \theta/\theta_{MAX} = 0$

$Re_f = 0.009$

$\mu = 126$ cp. $\rho = 1.05$ g/cc.

$c = 3.4$ cm/sec

FIGURE 11 PRESSURE-TIME TRACES

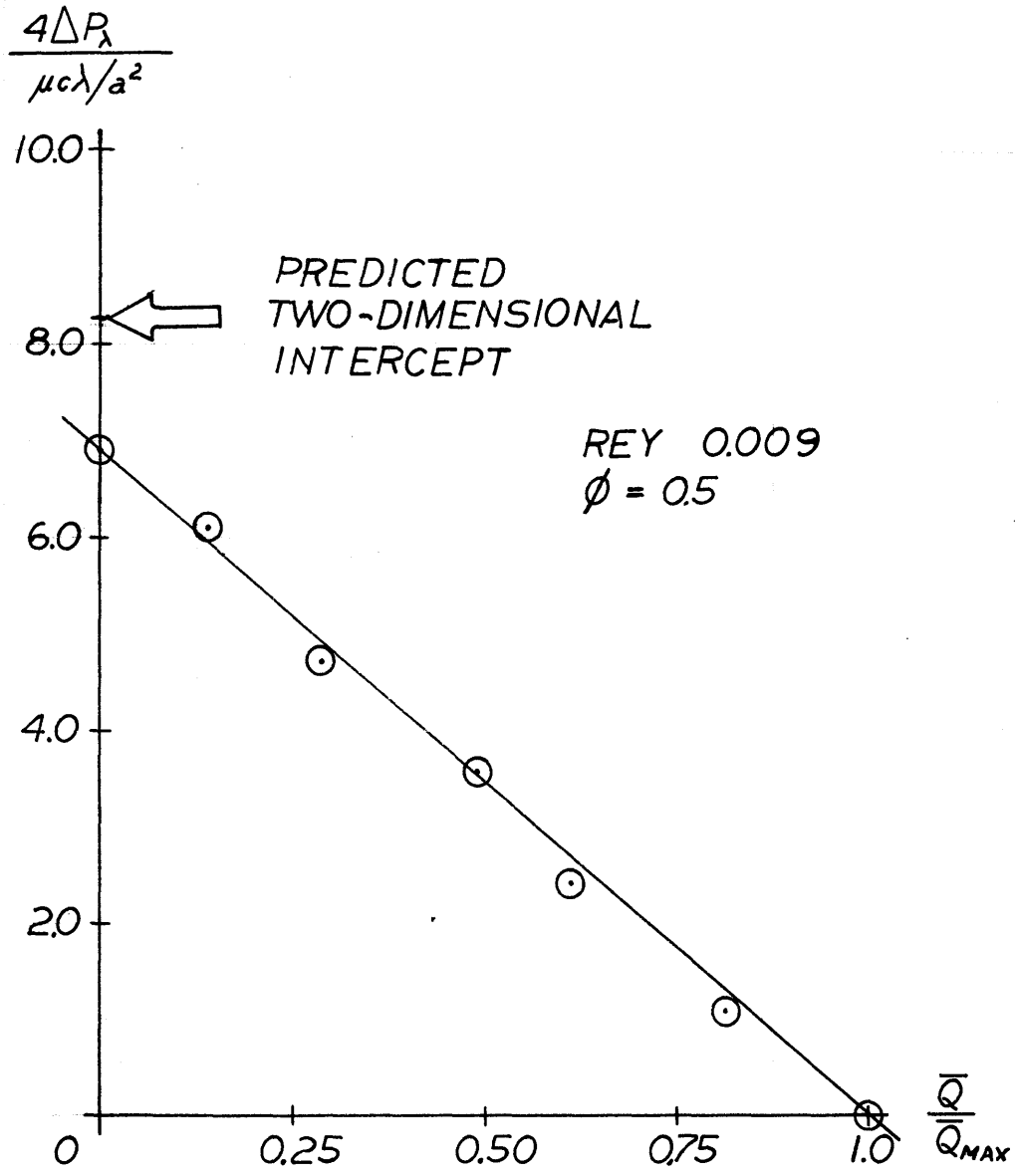

FIGURE 12 $\Delta P_\lambda - \bar{Q}$ GRAPH

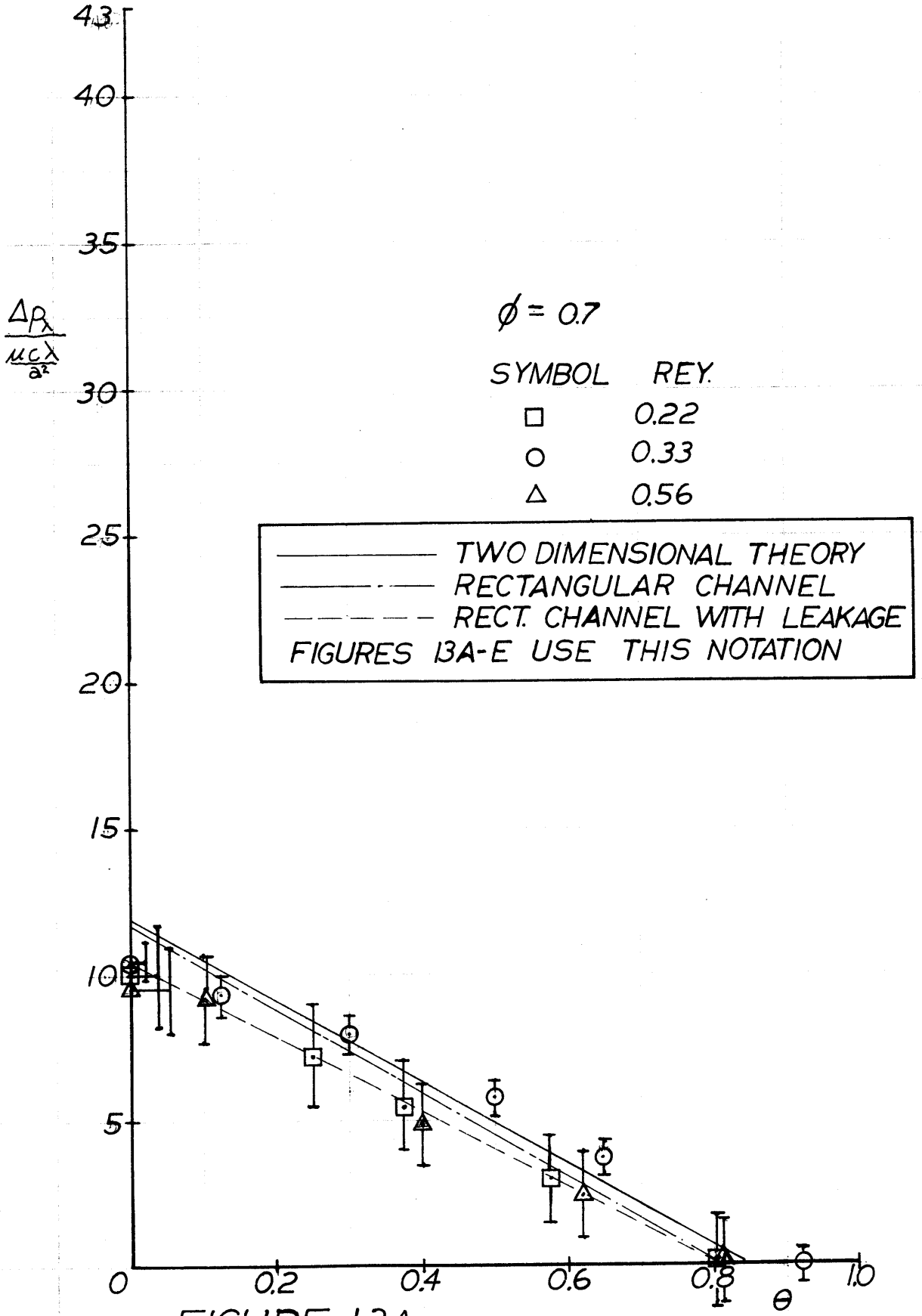
43
40
35
30
25
20
15
10
5
0
0.2
0.4
0.6
0.8
1.0
θ
$\frac{\Delta p_\lambda}{\frac{\mu c \lambda}{a^2}}$
$\phi = 0.7$
SYMBOL REY.
□ 0.22
○ 0.33
△ 0.56
TWO DIMENSIONAL THEORY
RECTANGULAR CHANNEL
RECT. CHANNEL WITH LEAKAGE
FIGURES 13A-E USE THIS NOTATION

FIGURE 13A

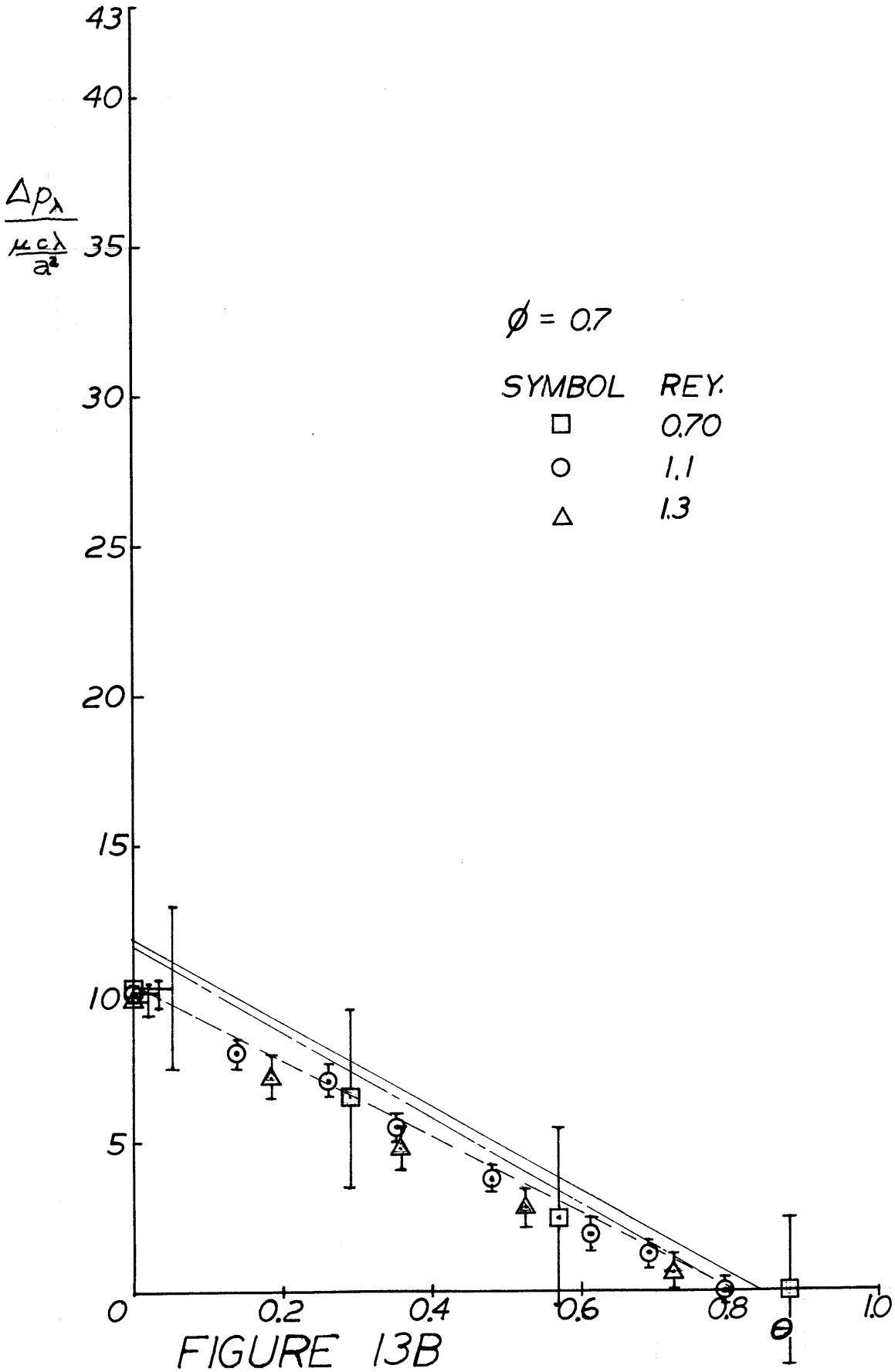
43
40
35
30
25
20
15
10
5
0
0.2
0.4
0.6
0.8
1.0
θ
$\frac{\Delta p_\lambda}{\frac{\mu c \lambda}{a^2}}$
ϕ = 0.7
SYMBOL REY.
0.70
1.1
1.3

FIGURE 13B

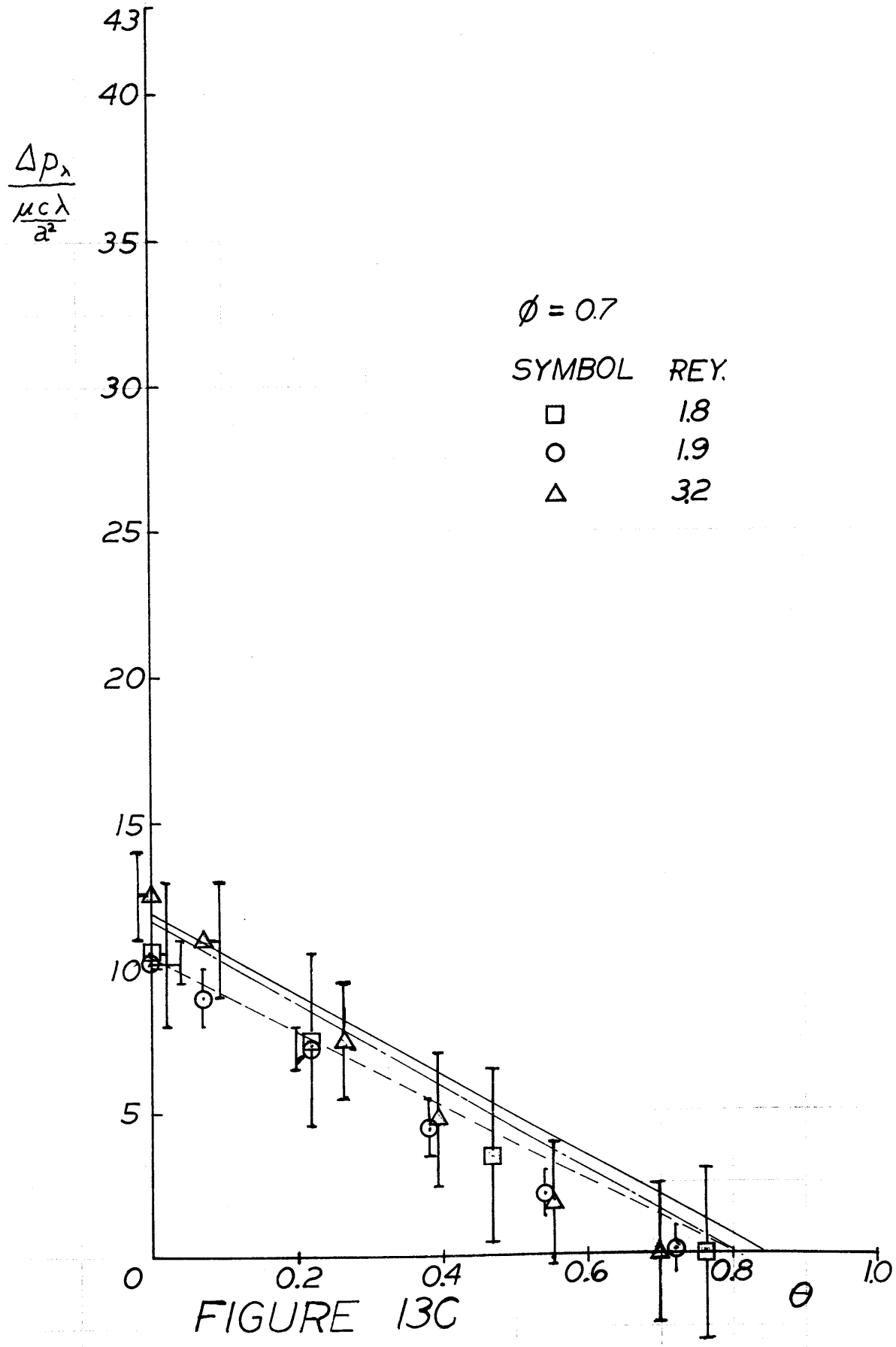
$\frac{\Delta p_\lambda}{\frac{\mu c \lambda}{a^2}}$
43
40
35
30
25
20
15
10
5
0
0.2
0.4
0.6
0.8
1.0
θ
ϕ = 0.7
SYMBOL
REY.
1.8
1.9
3.2

FIGURE 13C

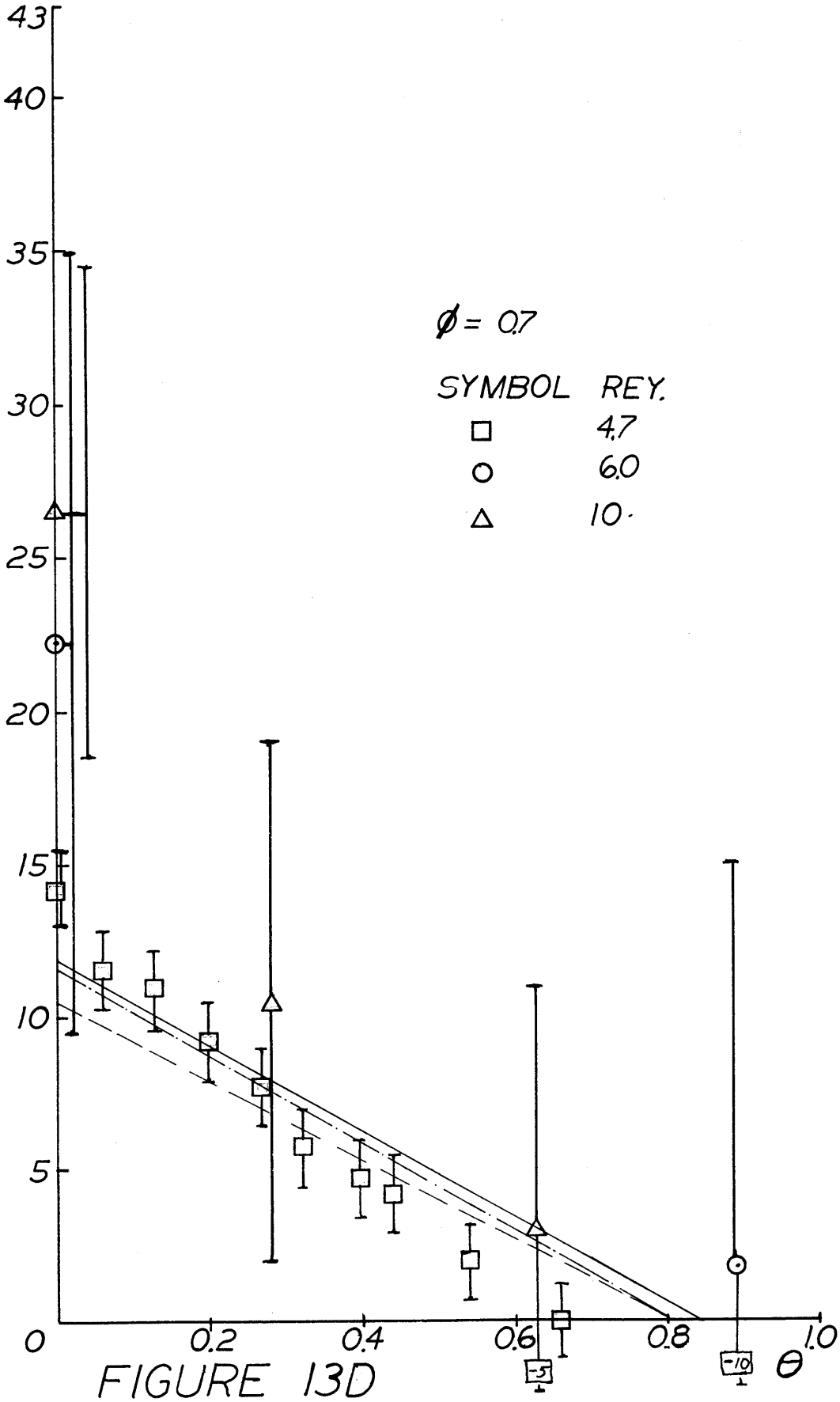
43
40
35
30
25
20
15
10
5
0
0.2
0.4
0.6
0.8
1.0
θ
-5
-10
Ø = 0.7
SYMBOL REY.
4.7
6.0
10.

FIGURE 13D

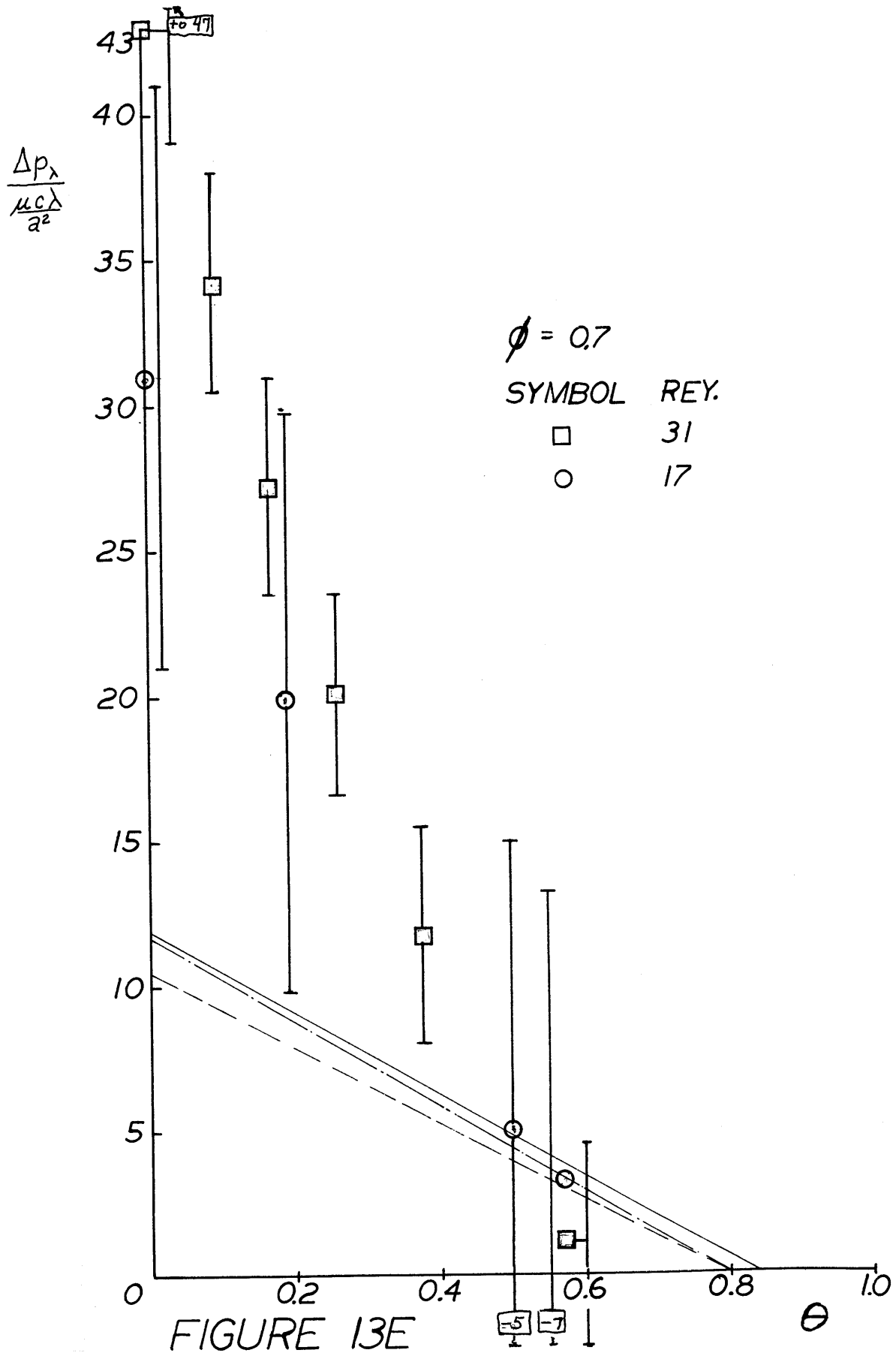
$\frac{\Delta p_\lambda}{\frac{\mu c \lambda}{a^2}}$
43
40
35
30
25
20
15
10
5
0
0.2
0.4
0.6
0.8
1.0
θ
+0.47
-5
-7
ϕ = 0.7
SYMBOL REY.
31
17

FIGURE 13E

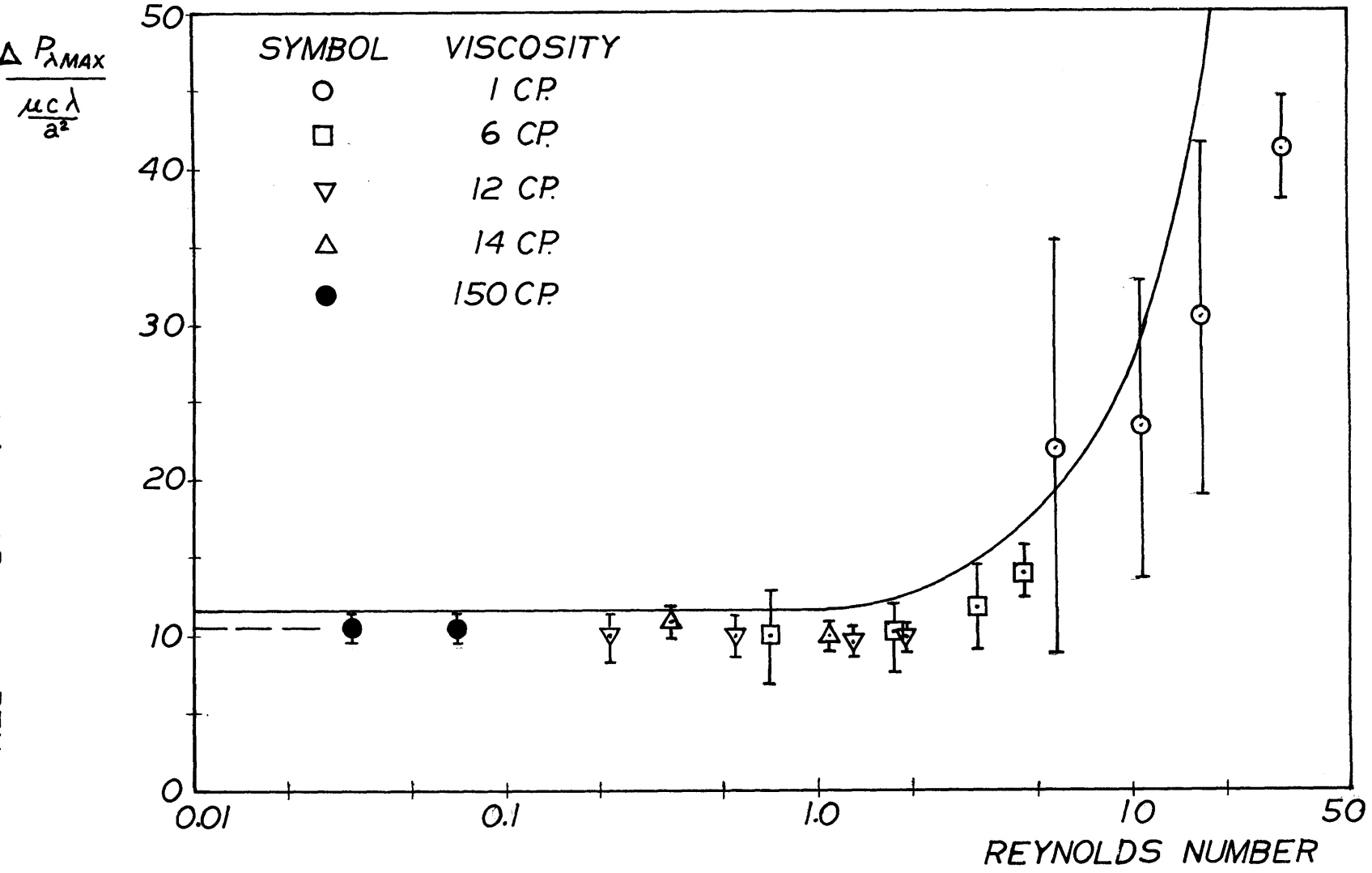

FIGURE 14 $\Delta P_{\lambda MAX}$ VS. REY.

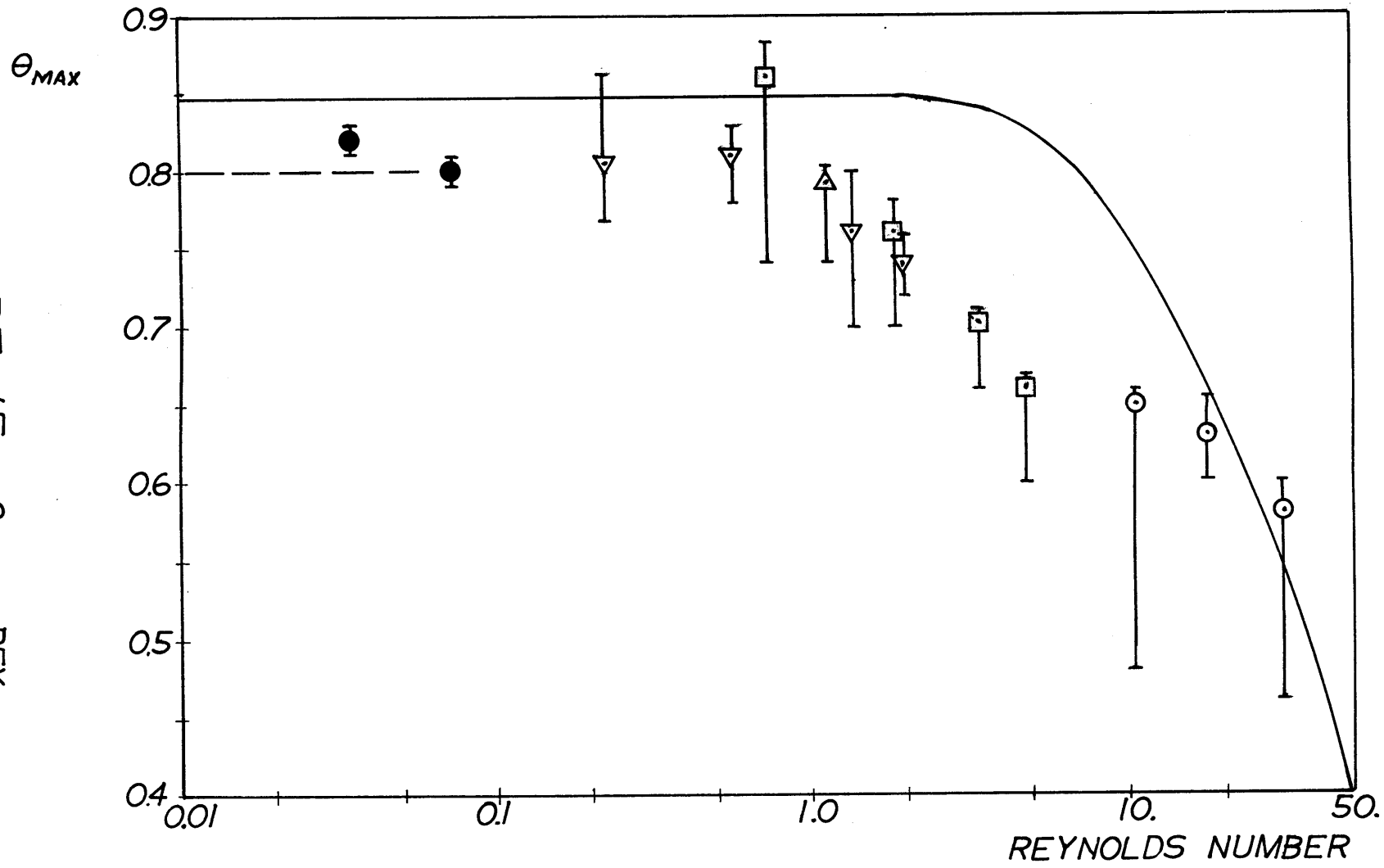

FIGURE 15 θ_{MAX} VS. REY.

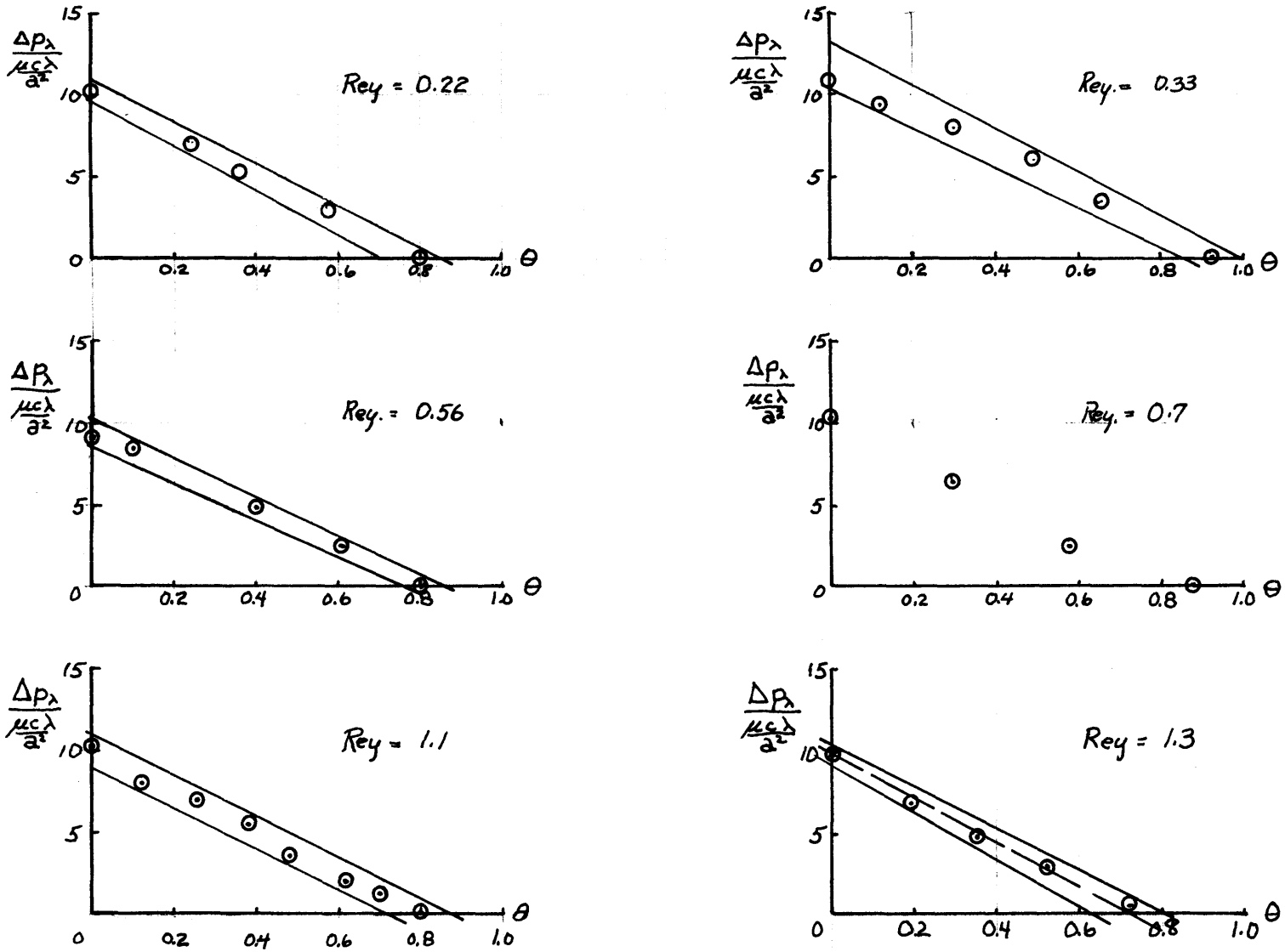

FIGURE 16A θ BAND LIMITS

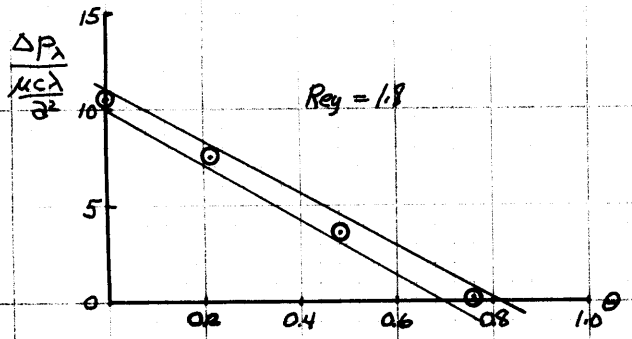

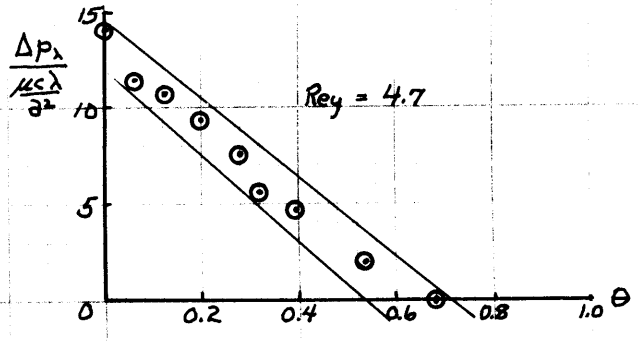

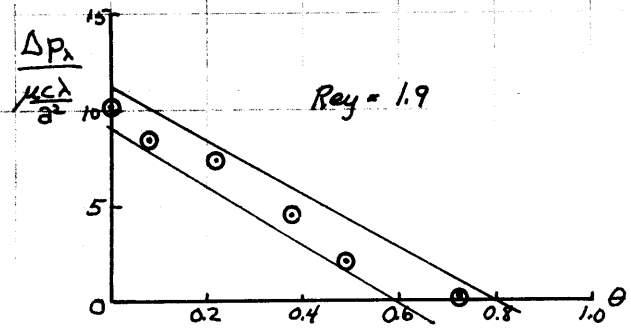

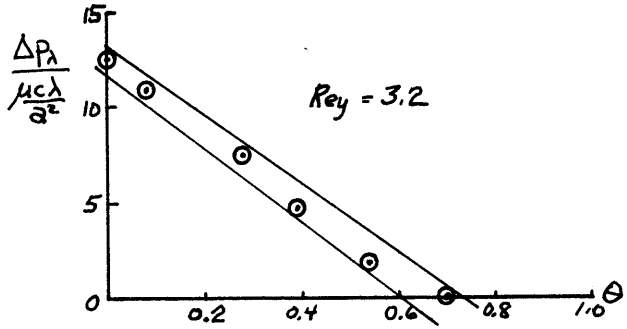

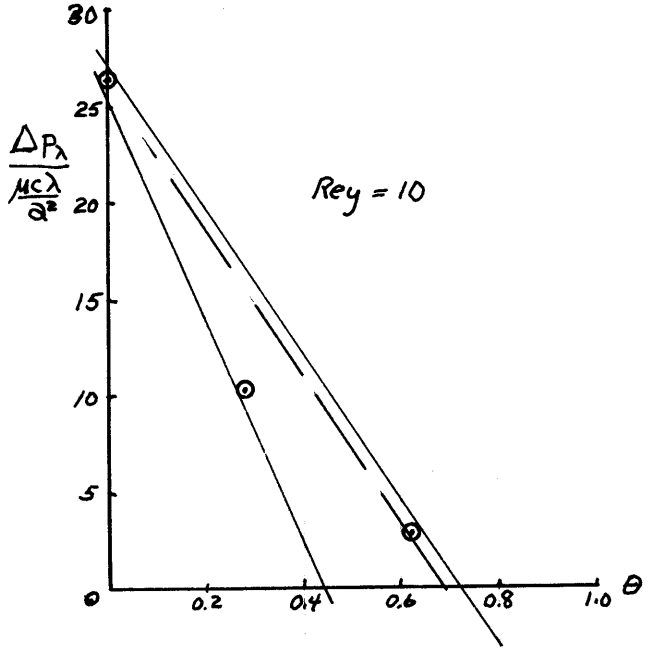

FIGURE 16B θ BAND LIMITS

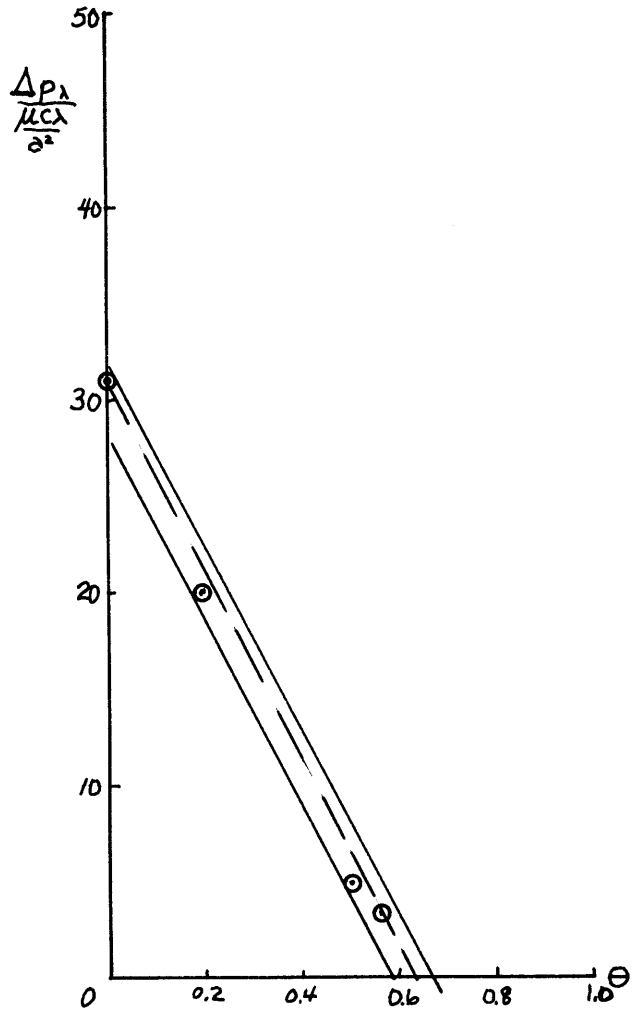

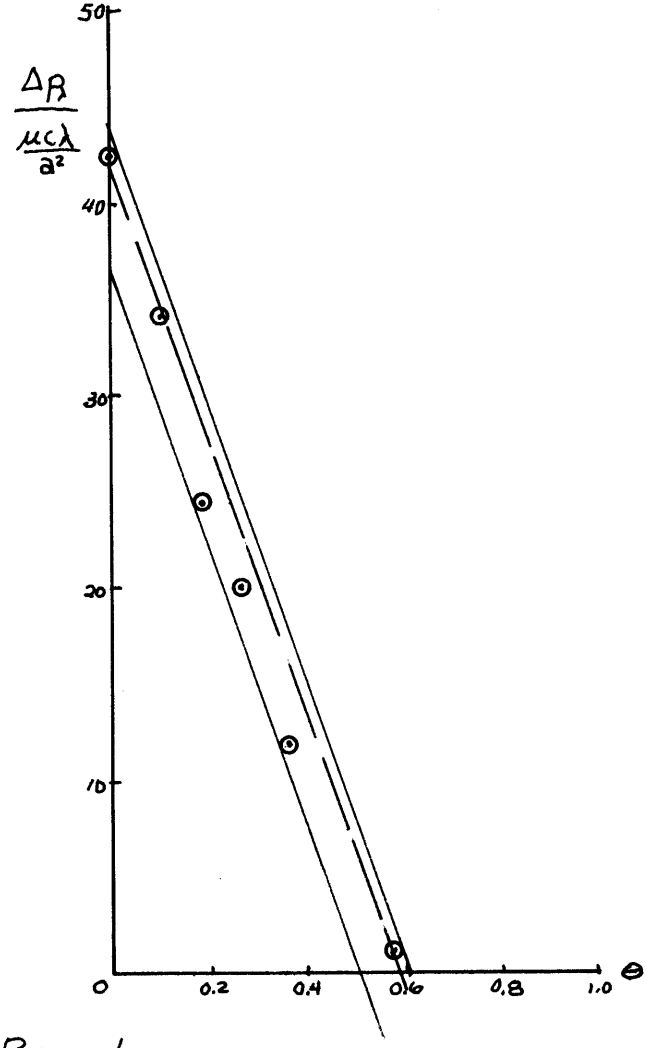

FIGURE 16C θ BAND LIMITS